Computers and Concrete, *Vol. 23, No. 3 (2019) 171-188*
DOI: https://doi.org/10.12989/cac.2019.23.3.171

Isogeometric analysis of gradient-enhanced damaged plasticity model for concrete

Jun Xu[a], Shuai Yuan[b] and Weizhen Chen[*]

Department of Bridge Engineering, Tongji University, Shanghai, China

(Received October 14, 2018, Revised March 2, 2019, Accepted March 5, 2019)

Abstract. This study proposed a new and efficient 2D damage-plasticity model within the framework of Isogeometric analysis (IGA) for the geometrically nonlinear damage analysis of concrete. Since concrete exhibits complicated material properties, two internal variables are introduced to measure the hardening/softening behavior of concrete in tension and compression, and an implicit gradient-enhanced formulation is adopted to restore the well-posedness of the boundary value problem. The numerical results calculated by the model is compared with the experimental data of three benchmark problems of plain concrete (three-point and four-point bending single-notched beams and four-point bending double-notched beam) to illustrate the geometrical flexibility, accuracy, and robustness of the proposed approach. In addition, the influence of the characteristic length on the numerical results of each problem is investigated.

Keywords: damaged plasticity model; concrete; isogeometric analysis; implicit gradient-enhanced formulation; characteristic length

1. Introduction

Computer-aided design (CAD) and computer-aided engineering (CAE) based on two platforms can only transmit information unidirectionally in the traditional finite element simulation. With the idea of isogeometric analysis (IGA), a seamless combination of CAD and CAE has been successfully implemented. IGA is proposed by Hughes *et al*. (2005) based on the idea of an isoparametric element in the finite element method. In IGA, the basic function of a non-uniform rational B-spline (NURBS) in computer-aided geometric design is used as a shape function for expressing the geometric model. While IGA has been extensively explored in mechanical and aerospace engineering applications (e.g., Cottrell *et al*. 2006, Bazilevs *et al*. 2008, de Borst *et al*. 2011, Anitescu *et al*. 2015, Jia *et al*. 2015, Nguyen *et al*. 2015, Bui *et al*. 2016, Thai *et al*. 2016), its application in classical civil engineering structures is relatively scarce. However, civil engineering designs are also commonly based on CAD data, and accurate geometric modeling capabilities of CAD basis functions can be exploited in such area (e.g., Ozbolt *et al*. 2007, Feist and Hofstetter 2007). The IGA also has advantages in the context of damage mechanics, which are commonly used for concrete materials given its high-order continuity, see e.g., the contributions in Borden *et al*. (2014) or Thai *et al*. (2016).

The typical failure modes of concrete are cracking in tension and crushing in compression. The failure process is characterized by irreversible deformations and degradations of material stiffness, thereby leading to tension and compression to strain-softening (e.g., Jelic *et al*. 2004). Thus, considering the properties of concrete materials as comprehensive as possible is an arduous task in the spatial refinement analysis of concrete structures. At present, constitutive models of concrete can be categorized into elastic models (e.g., Darwin and Pecknold 1977, Elwi and Murray 1979), plasticity models (e.g., Chen and Chen 1975, Han and Chen 1985), damage models (e.g., Loland 1980, Mazars and Pijaudier-Cabot 1989), and damage-plasticity models (e.g., Lee and Fenves 1998, Rabczuk and Eibl 2003). Among them, damage-plasticity models can describe comprehensively the complex mechanical properties of concrete materials. Plasticity is established in the effective stress space, and damage is used to reduce effective stress to nominal stress. These models can be based on a scalar (isotropic) damage (e.g., Lee and Fenves 1998, Rabczuk and Eibl 2003, Grassl and Jirasek 2006a) or tensor (anisotropic) damage (e.g., Rabczuk and Eibl 2006, Voyiadjis *et al*. 2008). The mathematical expression of anisotropic damage is complex and difficult to combine with plastic parts; thus, the damage is typically considered isotropy.

However, a local damage-plasticity model for concrete can lead to localization on a set of measure zeros (e.g., Bazant *et al*. 1984, Bazant 1991), which finally yield mesh-dependent results. Accordingly, several approaches have been developed to restore the well-posedness of the boundary value problem and alleviate this mesh dependency, such as gradient models (e.g., de Borst *et al*. 1996), nonlocal models (e.g., Bazant and Jirasek 2002, Rabczuk *et al*. 2005), smeared crack models (e.g., Rots *et*

∗Corresponding author, Professor
E-mail: tongji_bridge611@126.com
[a]Ph.D.
E-mail: jxuun@tongji.edu.cn
[b]Ph.D. Student
E-mail: 1432206@tongji.edu.cn

ISSN: 1598-8198 (Print), 1598-818X (Online)

al. 1985), and phase field approaches for fracture (e.g., Miehe *et al*. 2010). All models introduce a characteristic length l_{ch}, which can typically be motivated physically (e.g., Bazant and Pijaudier-Cabot 1989). Nonlocal theory can regularize a boundary value problem of a local model and can effectively eliminate its sensitivity, thereby resulting in a mesh size and arrangement form of the analysis region, which is an improved method. In nonlocal models, the state variable at any point $\mathbf{x}$ within an analysis domain Ω is not only determined by a local state parameter $f(\mathbf{x})$ at the point itself but also by neighboring points $\mathbf{y}$ within a certain range of the domain that has the point as the center.

$$\bar{f}(\mathbf{x}) = \frac{\int_{\Omega} \psi(\mathbf{x},\mathbf{y}) \cdot f(\mathbf{y})\, \mathrm{d}\Omega}{\int_{\Omega} \psi(\mathbf{x},\mathbf{y})\, \mathrm{d}\Omega} \tag{1}$$

where $\bar{f}(\mathbf{x})$ is the nonlocal variable at point $\mathbf{x}$; $\psi(\mathbf{x},\mathbf{y})$ is the weight function, which includes l_{ch}. Kröner (1967) and Eringen and Edelen (1972) incorporated nonlocal terms through integral equations for the elastic material model.

Pijaudier-Cabot and Bazant (1987) and Bazant and Pijaudier-Cabot (1988) introduced the philosophy of nonlocal theory to the studies of continuum damage mechanics, in which various models of nonlocal damage are developed. Generally, these models can be divided into two types, namely, integral and gradient-enhanced. A numerical implementation of the integral formulation (e.g., Bazant and Jirasek 2002) requires a global weighted averaging on every Gauss point within each local iteration step of the stress update, which is not only computationally inefficient but also difficult in linearizing an incremental equilibrium equation. The gradient-enhanced type approximates an integral formulation using a truncated Taylor series expansion, which can make the expression and application more flexible. Aifantis (1984) suggested a gradient approach to describe plastic instability problems; recently, gradient-enhanced models have been developed by subsequent researchers (e.g., Pamin 1994, de Borst and Pamin 1996, Peerlings *et al*. 1996a, Engelen *et al*. 2003, Dorgan and Voyiadjis 2006, Al-Rub and Voyiadjis 2009).

In the context of damage mechanics, high-order flexibility and continuity can be achieved through IGA method (e.g., Verhoosel *et al*. 2011, Borden *et al*. 2014, Thai *et al*. 2016). Therefore, if the gradient-enhanced damage-plasticity model of concrete can be analyzed under an IGA framework, then accurate damage-plasticity results can be obtained, and the calculation can be significantly simplified. The present study proposes a gradient-enhanced damage-plasticity model for concrete in the IGA framework. First, the IGA and the constitutive framework of the damage-plasticity model are introduced, and a second-order implicit gradient formulation is discussed, thereby regularizing the local internal variables as a localization limiter. Second, the equilibrium equation and derivation of the final discrete system of equations are presented. Finally, three numerical examples are described to verify the effectiveness of the proposed approach.

2. Basic concepts of isogeometric analysis

2.1 B-spline and NURBS basis functions

A pth-order B-spline curve is defined on an open knot vector $\Xi = \{\xi_1, \xi_2, \ldots, \xi_{n+p+1}\}$ $(\xi_1 \le \xi_2 \le \cdots \le \xi_i \le \xi_{i+1} \le \cdots \le \xi_{n+p+1})$ in accordance with the following equation

$$\mathbf{C}(\xi) = \sum_{i=1}^{n} N_{i,p}(\xi)\mathbf{B}_i \tag{2}$$

where $\mathbf{B}_i = \{B_i\}_{i=1}^{n}$ and $\{N_{i,p}(\xi)\}_{i=1}^{n}$ are the control points and B-spline basis functions, correspondingly; n and p are the number and polynomial order of the basis functions, respectively. $N_{i,p}(\xi)$ is defined by the following Cox-de-Boor recursion formula

For $p = 0$,

$$\boldsymbol{N_{i,0}(\xi)} = \begin{cases} \mathbf{1} & \boldsymbol{\xi_i \le \xi < \xi_{i+1}} \\ \mathbf{0} & \textbf{otherwise} \end{cases} \tag{3}$$

For $p \ge 1$,

$$\begin{aligned} \boldsymbol{N_{i,p}(\xi)} &= \frac{\boldsymbol{\xi - \xi_i}}{\boldsymbol{\xi_{i+p} - \xi_i}} \boldsymbol{N_{i,p-1}(\xi)} \\ &+ \frac{\boldsymbol{\xi_{i+p+1} - \xi}}{\boldsymbol{\xi_{i+p+1} - \xi_{i+1}}} \boldsymbol{N_{i+1,p-1}(\xi)} \end{aligned} \tag{4}$$

The NURBS basis functions can be obtained from B-splines using the following formula

$$\boldsymbol{R_i^p(\xi)} = \frac{\boldsymbol{N_{i,p}(\xi)\omega_i}}{\boldsymbol{W(\xi)}} = \frac{\boldsymbol{N_{i,p}(\xi)\omega_i}}{\boldsymbol{\sum_{\hat{i}=1}^{n} N_{\hat{i},p}(\xi)\omega_{\hat{i}}}} \tag{5}$$

where $\{\omega_i\}_{i=1}^{n}$ $(\omega_i > 0)$ are the weight functions. A pth-order NURBS curve can be constructed by using the linear combination of the NURBS basis functions $\{R_i^p(\xi)\}_{i=1}^{n}$ and control points $\{B_i\}_{i=1}^{n}$.

$$\boldsymbol{C(\xi)} = \sum_{\boldsymbol{i=1}}^{\boldsymbol{n}} \boldsymbol{R_i^p(\xi) B_i} \tag{6}$$

Moreover, a NURBS surface can be constructed as a tensor product of the three NURBS basis functions on the directions of ξ and η.

$$\boldsymbol{S(\xi,\eta)} = \sum_{\boldsymbol{i=1}}^{\boldsymbol{n}} \sum_{\boldsymbol{j=1}}^{\boldsymbol{m}} \boldsymbol{R_{i,j}^{p,q}(\xi,\eta) B_{i,j}} \tag{7}$$

$$\boldsymbol{R_{i,j}^{p,q}(\xi,\eta)} = \frac{\boldsymbol{N_{i,p}(\xi) M_{j,q}(\eta)\omega_{i,j}}}{\boldsymbol{\sum_{\hat{i}=1}^{n}\sum_{\hat{j}=1}^{m} N_{\hat{i},p}(\xi) M_{\hat{j},q}(\eta)\omega_{\hat{i},\hat{j}}}} \tag{8}$$

where $\{N_{i,p}(\xi)\}_{i=1}^{n}$ and $\{M_{j,q}(\eta)\}_{j=1}^{m}$ are the B-spline basis functions defined on the knot vectors of $\Xi^1 = \{\xi_1, \xi_2, \ldots, \xi_{n+p+1}\}$ and $\Xi^2 = \{\eta_1, \eta_2, \ldots, \eta_{m+q+1}\}$, correspondingly; $\mathbf{B}_{i,j}$ is the set of control points.

2.2 IGA based on NURBS

Considering that the domain Ω consists of *ne* NURBS

elements, three spaces, i.e. the parent space $\widetilde{\Omega}^{\text{ele}}$, the parametric space $\widehat{\Omega}^{\text{ele}}$ and the physical space Ω^{ele} are defined by the local, knot and Cartesian coordinates, respectively

$$\widetilde{\boldsymbol{\Omega}}^{\boldsymbol{ele}} = \left[\tilde{\xi}_i, \tilde{\xi}_{i+1}\right] \otimes \left[\tilde{\eta}_j, \tilde{\eta}_{j+1}\right] = [-\mathbf{1}, \mathbf{1}] \otimes [-\mathbf{1}, \mathbf{1}] \quad (9)$$

$$\widehat{\boldsymbol{\Omega}}^{\mathbf{ele}} = [\xi_i, \xi_{i+1}] \otimes \left[\eta_j, \eta_{j+1}\right], \ \xi_i \neq \xi_{i+1}, \ \eta_j \neq \eta_{j+1} \quad (10)$$

$$\boldsymbol{\Omega}^{\mathbf{ele}} = [x_i, x_{i+1}] \otimes \left[y_j, y_{j+1}\right], \ x_i \neq x_{i+1}, \ y_j \neq y_{j+1} \quad (11)$$

The mapping of the parametric space → parent space and physical space → parametric space are defined as the mapping ϕ_1 and ϕ_2, correspondingly. For ϕ_2, the NURBS surface $\mathrm{d}\Omega^{\text{ele}}$ constructed by $\mathrm{d}\boldsymbol{\xi}$ and $\mathrm{d}\boldsymbol{\eta}$ satisfies the following equation

$$\begin{aligned} d\boldsymbol{\Omega}^{ele} &= d\boldsymbol{\xi} \otimes d\boldsymbol{\eta} = \begin{vmatrix} \dfrac{\partial x}{\partial \xi} & \dfrac{\partial y}{\partial \xi} \\ \dfrac{\partial x}{\partial \eta} & \dfrac{\partial y}{\partial \eta} \end{vmatrix} d\boldsymbol{\xi} d\boldsymbol{\eta} \\ &= |\boldsymbol{J}_2| \, d\boldsymbol{\xi} d\boldsymbol{\eta} = |\boldsymbol{J}_2| \, d\widehat{\boldsymbol{\Omega}}^{ele} \end{aligned} \quad (12)$$

where $\mathbf{J}_2 = \partial(x, y)/\partial(\xi, \eta)$ is the Jacobian matrix in ϕ_2.

For ϕ_1, the NURBS surface $\mathrm{d}\widehat{\Omega}^{\text{ele}}$ constructed by $\mathrm{d}\tilde{\boldsymbol{\xi}}$ and $\mathrm{d}\tilde{\boldsymbol{\eta}}$ satisfies

$$\begin{aligned} d\widehat{\boldsymbol{\Omega}}^{ele} &= d\tilde{\boldsymbol{\xi}} \otimes d\tilde{\boldsymbol{\eta}} = \begin{vmatrix} \dfrac{\partial \xi}{\partial \tilde{\xi}} & \dfrac{\partial \eta}{\partial \tilde{\xi}} \\ \dfrac{\partial \xi}{\partial \tilde{\eta}} & \dfrac{\partial \eta}{\partial \tilde{\eta}} \end{vmatrix} d\tilde{\boldsymbol{\xi}} d\tilde{\boldsymbol{\eta}} \\ &= |\boldsymbol{J}_1| \, d\tilde{\boldsymbol{\xi}} d\tilde{\boldsymbol{\eta}} = |\boldsymbol{J}_1| \, d\widetilde{\boldsymbol{\Omega}}^{ele} \end{aligned} \quad (13)$$

where $\mathbf{J}_1 = \partial(\xi, \eta)/\partial\left(\tilde{\xi}, \tilde{\eta}\right)$ is the Jacobian matrix for ϕ_1.

The integral of a function $\boldsymbol{\mathcal{B}}$ (e.g., stiffness matrix) on Ω can be obtained by using

$$\begin{aligned} \int_{\boldsymbol{\Omega}} \boldsymbol{\mathcal{B}}(\boldsymbol{x}, \boldsymbol{y}) d\boldsymbol{\Omega} &= \sum_{\boldsymbol{ele}=\mathbf{1}}^{\boldsymbol{ne}} \int_{\boldsymbol{\Omega}^{ele}} \boldsymbol{\mathcal{B}}(\boldsymbol{x}, \boldsymbol{y}) d\boldsymbol{\Omega}^{ele} \\ &= \sum_{\boldsymbol{ele}=\mathbf{1}}^{\boldsymbol{ne}} \int_{\widetilde{\boldsymbol{\Omega}}^{ele}} \boldsymbol{\mathcal{B}}\left(\tilde{\boldsymbol{\xi}}, \tilde{\boldsymbol{\eta}}\right) |\boldsymbol{J}| d\widetilde{\boldsymbol{\Omega}}^{ele} \end{aligned} \quad (14)$$

where $|\mathbf{J}| = |\mathbf{J}_2| \cdot |\mathbf{J}_1|$.

3. Framework of the local concrete model

3.1 Basic equations

The basic equation for the damage-plasticity model of concrete is expressed as

$$\boldsymbol{\sigma} = (\mathbf{1} - \boldsymbol{d})\bar{\boldsymbol{\sigma}} = (\mathbf{1} - \boldsymbol{d})\boldsymbol{D}^{\boldsymbol{e}}\boldsymbol{\varepsilon}^{\boldsymbol{e}} = (\mathbf{1} - \boldsymbol{d})\boldsymbol{D}^{\boldsymbol{e}}(\boldsymbol{\varepsilon} - \boldsymbol{\varepsilon}^{\boldsymbol{p}}) \quad (15)$$

where $\boldsymbol{\sigma}$ and $\bar{\boldsymbol{\sigma}}$ are the nominal and effective stresses, respectively; d is the damage factor. Since the damage-plasticity model is based on a scalar (isotropic) damage, it is generally believed that d is driven by the internal variables $\boldsymbol{\kappa}$ of concrete.

$$\boldsymbol{d} = \boldsymbol{d}(\boldsymbol{\kappa}) \quad (16)$$

According to the plasticity theory, the total strain of concrete is decomposed into the elastic part $\boldsymbol{\varepsilon}^{\text{e}}$ and the plastic part $\boldsymbol{\varepsilon}^{\text{p}}$.

$$\boldsymbol{\varepsilon} = \boldsymbol{\varepsilon}^{\boldsymbol{e}} + \boldsymbol{\varepsilon}^{\boldsymbol{p}} \quad (17)$$

Only the elastic part is assumed to cause damage; thus, the damaged part is included in $\boldsymbol{\varepsilon}^{\text{e}}$. The increment in plastic strain can be calculated using the following equation

$$\dot{\boldsymbol{\varepsilon}}^{\boldsymbol{p}} = \dot{\boldsymbol{\lambda}}^{\boldsymbol{p}} \boldsymbol{m}(\bar{\boldsymbol{\sigma}}, \boldsymbol{\kappa}) = \dot{\boldsymbol{\lambda}}^{\boldsymbol{p}} \frac{\boldsymbol{\partial \Phi}(\bar{\boldsymbol{\sigma}}, \boldsymbol{\kappa})}{\boldsymbol{\partial \bar{\sigma}}} \quad (18)$$

where $\dot{\lambda}^{\text{p}}$ is the plastic multiplier, $\mathbf{m}$ is the flow vector, Φ is the plastic potential, and $\dot{(\ )}$ denotes the derivative with respect to time.

The increment in internal variables can be calculated as follows

$$\dot{\boldsymbol{\kappa}} = \dot{\boldsymbol{\lambda}}^{\boldsymbol{p}} \boldsymbol{h}(\bar{\boldsymbol{\sigma}}, \boldsymbol{\kappa}) \quad (19)$$

where $\mathbf{h}$ is the plastic modulus.

The plastic multiplier is determined from the loading-unloading conditions.

$$\dot{\boldsymbol{\lambda}}^{\boldsymbol{p}} \geq \mathbf{0}, \boldsymbol{F}(\bar{\boldsymbol{\sigma}}, \boldsymbol{\kappa}) \leq \mathbf{0} \ \textbf{with} \ \dot{\boldsymbol{\lambda}}^{\boldsymbol{p}} \boldsymbol{F} = \mathbf{0} \quad (20)$$

where F is the yield function.

3.2 Internal variables

The internal variable κ is used to record the loading history of concrete, which is similar to the hardening variable in the elastic-plastic model (e.g., Lubliner *et al*. 1989). κ can be measured by either the accumulative plastic work or the accumulative equivalent plastic strain. In this study, κ is defined as follows

$$\boldsymbol{\kappa} = \int_{\mathbf{0}}^{\boldsymbol{t}} \dot{\boldsymbol{\kappa}} \boldsymbol{dt} \Leftrightarrow \tilde{\boldsymbol{\varepsilon}}^{\boldsymbol{p}} = \int_{\mathbf{0}}^{\boldsymbol{t}} \dot{\tilde{\boldsymbol{\varepsilon}}}^{\boldsymbol{p}} \boldsymbol{dt} \quad (21)$$

where $\tilde{\varepsilon}^{\text{p}}$ is the equivalent plastic strain.

The material properties of concrete under tension and compression are different. Thus, using two internal variables κ_t and κ_c related to hardening/softening behavior of concrete under tension and compression, correspondingly, is necessary.

$$\boldsymbol{\kappa} = (\boldsymbol{\kappa_t} \quad \boldsymbol{\kappa_c})^{\boldsymbol{T}} = \left(\tilde{\boldsymbol{\varepsilon}}_{\boldsymbol{t}}^{\boldsymbol{p}} \quad \tilde{\boldsymbol{\varepsilon}}_{\boldsymbol{c}}^{\boldsymbol{p}}\right)^{\boldsymbol{T}} \quad (22)$$

where $\tilde{\varepsilon}_t^{\text{p}}$ and $\tilde{\varepsilon}_c^{\text{p}}$ are the tensile and compressive equivalent plastic strains, respectively.

3.3 Plasticity criterion

The yield surface of the concrete is described by the three-parameter Barcelona function (e.g., Lee and Fenves 1998).

$$\begin{aligned} \boldsymbol{F} = \frac{\mathbf{1}}{\mathbf{1} - \boldsymbol{\alpha_F}} \Bigg(& \boldsymbol{\alpha_F} \bar{\boldsymbol{I}}_{\mathbf{1}} + \sqrt{\mathbf{3}\bar{\boldsymbol{J}}_{\mathbf{2}}} + \boldsymbol{\beta_F}(\boldsymbol{\kappa}) \langle \hat{\bar{\boldsymbol{\sigma}}}_{\boldsymbol{max}} \rangle \\ & - \boldsymbol{\gamma_F} \langle -\hat{\bar{\boldsymbol{\sigma}}}_{\boldsymbol{max}} \rangle \Bigg) - \bar{\boldsymbol{c}}_{\boldsymbol{c}}(\boldsymbol{\kappa_c}) \end{aligned} \quad (23)$$

with

$$\boldsymbol{\alpha_F} = \frac{\boldsymbol{\theta} - \mathbf{1}}{\mathbf{2}\boldsymbol{\theta} - \mathbf{1}}, \ \mathbf{0} \leq \boldsymbol{\alpha_F} \leq \mathbf{5}$$

$$\boldsymbol{\beta_F(\kappa)} = \frac{\bar{\boldsymbol{c}}_{\boldsymbol{c}}(\boldsymbol{\kappa_c})}{\bar{\boldsymbol{c}}_{\boldsymbol{t}}(\boldsymbol{\kappa_t})}(\mathbf{1}-\boldsymbol{\alpha_F}) - (\mathbf{1}+\boldsymbol{\alpha_F})$$

$$\boldsymbol{\gamma_F} = \frac{\mathbf{3}(\mathbf{1}-\boldsymbol{K_c})}{\mathbf{2}\boldsymbol{K_c}-\mathbf{1}}$$

where $\bar{I}_1$ and $\bar{J}_2$ are the first stress invariant and second deviatoric stress invariant computed by the effective stress tensor $\bar{\boldsymbol{\sigma}}$, correspondingly. $\hat{\bar{\sigma}}_{\max}$ is the maximum principal effective stress, with $\langle x\rangle = (x+|x|)/2$, and $\theta = f_{b0}/f_{c0}$, where f_{c0} and f_{b0} are the uniaxial and biaxial compressive yield strengths of concrete, respectively; $\bar{c}_c(\kappa_c) = -\bar{\sigma}_c(\kappa_c) > 0$ and $\bar{c}_t(\kappa_t) = \bar{\sigma}_t(\kappa_t) > 0$ are the effective tensile and compressive cohesion stresses, correspondingly; the parameter K_c controls the projection of the yield function on the deviatoric plane, which must satisfy $0.5 \le K_c \le 1.0$. If $K_c = 1.0$, then the projection shape of the yield function on the deviatoric plane is circular, which is similar to the Drucker-Prager criterion; if $K_c = 0.5$, then the projection shape of the yield function on the deviatoric plane is triangular, which is similar to the Rankine criterion. In this study, $\theta = 1.16$, and $K_c = 2/3$ for all numerical examples.

The plastic potential is described by a hyperbolic form of the Drucker-Prager function (e.g., Saritas and Filippou 2009).

$$\boldsymbol{\Phi} = \sqrt{\left(\boldsymbol{\rho_p f_{t0}\tan\varphi}\right)^2 + \mathbf{3}\bar{\boldsymbol{J}}_{\mathbf{2}}} + \left(\frac{\boldsymbol{\tan\varphi}}{\mathbf{3}}\right)\bar{\boldsymbol{I}}_{\mathbf{1}} \tag{24}$$

where φ is the dilation angle that is typically used as $\pi/6$, f_{t0} is the uniaxial tensile yield strength, and ρ_p is the eccentricity parameter and is frequently considered 0.1. The stiffness matrix of concrete becomes asymmetric given the non-associated flow rule.

A plastic modulus is defined as follows

$$\boldsymbol{h}(\hat{\bar{\boldsymbol{\sigma}}},\boldsymbol{\kappa}) = \begin{pmatrix} \boldsymbol{r}(\hat{\bar{\boldsymbol{\sigma}}}) & \mathbf{0} & \mathbf{0} \\ \mathbf{0} & \mathbf{0} & -\left(\mathbf{1}-\boldsymbol{r}(\hat{\bar{\boldsymbol{\sigma}}})\right) \end{pmatrix} \cdot \frac{\boldsymbol{\partial\Phi}}{\boldsymbol{\partial}\hat{\bar{\boldsymbol{\sigma}}}} = \begin{pmatrix} \boldsymbol{r}(\hat{\bar{\boldsymbol{\sigma}}}) \cdot \dfrac{\boldsymbol{\partial\Phi}}{\boldsymbol{\partial}\hat{\bar{\boldsymbol{\sigma}}}_{\mathbf{1}}} \\ -\left(\mathbf{1}-\boldsymbol{r}(\hat{\bar{\boldsymbol{\sigma}}})\right) \cdot \dfrac{\boldsymbol{\partial\Phi}}{\boldsymbol{\partial}\hat{\bar{\boldsymbol{\sigma}}}_{\mathbf{3}}} \end{pmatrix} \tag{25}$$

where

$$\boldsymbol{r}(\hat{\bar{\boldsymbol{\sigma}}}) = \begin{cases} \mathbf{0} & \hat{\bar{\boldsymbol{\sigma}}} = \mathbf{0} \\ \left(\sum_{i=1}^{3}\langle\hat{\bar{\boldsymbol{\sigma}}}_i\rangle\right) \Big/ \left(\sum_{i=1}^{3}|\hat{\bar{\boldsymbol{\sigma}}}_i|\right) & \textbf{otherwise} \end{cases} \tag{26}$$

The substitution of Eq. (25) into Eq.(19) yields

$$\dot{\boldsymbol{\kappa}} = \begin{pmatrix} \dot{\boldsymbol{\kappa}}_t \\ \dot{\boldsymbol{\kappa}}_c \end{pmatrix} = \dot{\boldsymbol{\lambda}}^p \begin{pmatrix} \boldsymbol{r}(\hat{\bar{\boldsymbol{\sigma}}}) \cdot \dfrac{\boldsymbol{\partial\Phi}}{\boldsymbol{\partial}\hat{\bar{\boldsymbol{\sigma}}}_{\mathbf{1}}} \\ -\left(\mathbf{1}-\boldsymbol{r}(\hat{\bar{\boldsymbol{\sigma}}})\right) \cdot \dfrac{\boldsymbol{\partial\Phi}}{\boldsymbol{\partial}\hat{\bar{\boldsymbol{\sigma}}}_{\mathbf{3}}} \end{pmatrix} = \begin{pmatrix} \boldsymbol{r}(\hat{\bar{\boldsymbol{\sigma}}}) \cdot \dot{\hat{\boldsymbol{\varepsilon}}}_{\mathbf{1}}^{\boldsymbol{p}} \\ -\left(\mathbf{1}-\boldsymbol{r}(\hat{\bar{\boldsymbol{\sigma}}})\right) \cdot \dot{\hat{\boldsymbol{\varepsilon}}}_{\mathbf{3}}^{\boldsymbol{p}} \end{pmatrix} \tag{27}$$

3.4 Damage criterion

Two damage variables, namely, d_t and d_c, are introduced to measure the tensile and compressive damage of concrete, which are driven by κ_t and κ_c, respectively.

$$\boldsymbol{d_t} = \boldsymbol{d}(\boldsymbol{\kappa_t}) = \boldsymbol{d}\left(\tilde{\boldsymbol{\varepsilon}}_{\boldsymbol{t}}^{\boldsymbol{p}}\right); \qquad \mathbf{0} \le \boldsymbol{d_t} \le \mathbf{1} \tag{28}$$

$$\boldsymbol{d_c} = \boldsymbol{d}(\boldsymbol{\kappa_c}) = \boldsymbol{d}\left(\tilde{\boldsymbol{\varepsilon}}_{\boldsymbol{c}}^{\mathbf{p}}\right); \qquad \mathbf{0} \le \boldsymbol{d_c} \le \mathbf{1} \tag{29}$$

The total damage of concrete is a combination of d_t and d_c (e.g., Saritas and Filippou 2009)

$$\boldsymbol{d} = \mathbf{1} - (\mathbf{1}-\boldsymbol{s_t d_c})(\mathbf{1}-\boldsymbol{s_c d_t}) \tag{30}$$

with

$$\boldsymbol{s_t} = \mathbf{1} - \boldsymbol{w_t}\boldsymbol{r}(\hat{\bar{\boldsymbol{\sigma}}}); \qquad \mathbf{0} \le \boldsymbol{w_t} \le \mathbf{1}$$

$$\boldsymbol{s_c} = \mathbf{1} - \boldsymbol{w_c}\left(\mathbf{1}-\boldsymbol{r}(\hat{\bar{\boldsymbol{\sigma}}})\right); \qquad \mathbf{0} \le \boldsymbol{w_c} \le \mathbf{1}$$

where w_t and w_c refer to the stiffness recovery factors in tension and compression, correspondingly. If compressive stiffness can be recovered upon crack closure when a load changes from tension to compression, and the tensile stiffness cannot be fully recovered as the load changes from compression to tension once crushing develops, then this property is reflected by considering $w_t = 0$ and $w_c = 1$.

On the basis of experimental data, Yu and Wu (2009) suggested that the plastic strain of concrete under uniaxial loading satisfies

$$\boldsymbol{\varepsilon}_{\aleph}^{\boldsymbol{p}} = \boldsymbol{\alpha}(\boldsymbol{\varepsilon}_{\aleph} - \boldsymbol{\varepsilon}_{\mathbf{0}\aleph})^{\boldsymbol{\beta}} \tag{31}$$

where $\alpha = 1.79$ and $\beta = 1.18$ are the material parameters (e.g., Yu and Wu 2009), $\varepsilon_{\aleph}$ is the total strain, $\varepsilon_{0\aleph}$ is the strain at the elastic limit, and $\aleph \in \{t, c\}$ indicates the stress state.

In our study, $\kappa_{\aleph} = \varepsilon_{\aleph}^{\mathrm{p}}$ for uniaxial loading; thus, the effective stress can be calculated as follows

$$\bar{\boldsymbol{\sigma}}_{\aleph}(\boldsymbol{\kappa}_{\aleph}) = \begin{cases} \boldsymbol{E}_{\aleph\mathbf{0}}\boldsymbol{\varepsilon}_{\aleph} & \boldsymbol{\kappa}_{\aleph} = \mathbf{0} \\ \boldsymbol{E}_{\aleph\mathbf{0}}\left[\boldsymbol{\varepsilon}_{\mathbf{0}\aleph} + \left(\dfrac{\boldsymbol{\kappa}_{\aleph}}{\boldsymbol{\alpha}}\right)^{\frac{\mathbf{1}}{\boldsymbol{\beta}}} - \boldsymbol{\kappa}_{\aleph}\right] & \boldsymbol{\kappa}_{\aleph} > \mathbf{0} \end{cases} \tag{32}$$

Moreover, Yu and Wu (2009) proposed the damage evolution law as follows

$$\boldsymbol{d}_{\aleph}(\boldsymbol{\kappa}_{\aleph}) = \begin{cases} \boldsymbol{d}_{\mathbf{0}\aleph} & \boldsymbol{\kappa}_{\aleph} = \mathbf{0} \\ \boldsymbol{d}_{\mathbf{0}\aleph} + \boldsymbol{A}_{\mathbf{1}\aleph}\left(\dfrac{\boldsymbol{\kappa}_{\aleph}}{\boldsymbol{\alpha}}\right)^{\frac{\boldsymbol{B}_{\mathbf{1}\aleph}}{\boldsymbol{\beta}}} & \boldsymbol{\kappa}_{\aleph} \le \boldsymbol{\kappa}_{\boldsymbol{f}\aleph} \\ \mathbf{1} - \dfrac{(\mathbf{1}-\boldsymbol{d}_{\boldsymbol{f}\aleph})\boldsymbol{\Pi}_{\aleph}^{\boldsymbol{B}_{\mathbf{2}\aleph}}}{\boldsymbol{A}_{\mathbf{2}\aleph}(\boldsymbol{\Pi}_{\aleph}-\mathbf{1})^{\boldsymbol{B}_{\mathbf{3}\aleph}}+\boldsymbol{\Pi}_{\aleph}} & \boldsymbol{\kappa}_{\aleph} > \boldsymbol{\kappa}_{\boldsymbol{f}\aleph} \end{cases} \tag{33}$$

with

$$\boldsymbol{\Pi}_{\aleph} = \frac{\boldsymbol{\varepsilon}_{\mathbf{0}\aleph} + \left(\dfrac{\boldsymbol{\kappa}_{\aleph}}{\boldsymbol{\alpha}}\right)^{\frac{\mathbf{1}}{\boldsymbol{\beta}}}}{\boldsymbol{\varepsilon}_{\boldsymbol{f}\aleph}}$$

where $d_{0\aleph}$ is the initial damage and is typically regarded as 0; $d_{f\aleph}$ is the damage at the peak strain $\varepsilon_{f\aleph}$; $A_{2\aleph}$ and $B_{3\aleph}$ are the parameters that control the softening shape of the nominal stress-strain curve; $A_{1\aleph}$, $B_{1\aleph}$, and $B_{2\aleph}$ are the parameters that can be derived in accordance with the

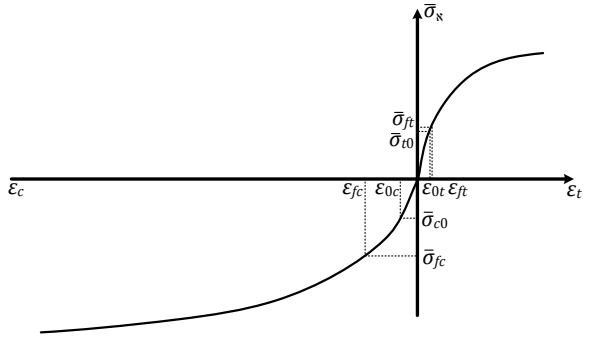

(a) Effective stress-strain curve

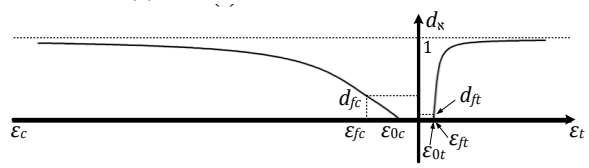

(b) Damage variable-strain curve

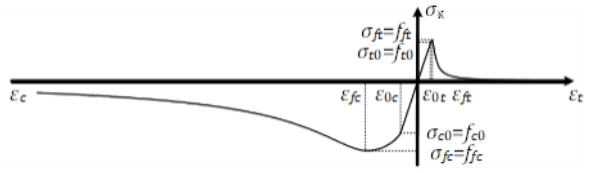

(c) Nominal stress-strain curve

Fig. 1 Evolution curves of effective stress, damage variable, and nominal stress

continuity requirements of the stress-strain curve.

$$\boldsymbol{B}_{1\aleph} = \frac{\boldsymbol{\lambda}_\aleph \bar{\boldsymbol{\sigma}}'_{f\aleph}\left(\boldsymbol{\varepsilon}_{f\aleph} - \boldsymbol{\varepsilon}_{0\aleph}\right)}{\bar{\boldsymbol{\sigma}}_{f\aleph}\left(\mathbf{1} - \boldsymbol{d}_{0\aleph} - \boldsymbol{\lambda}_\aleph\right)} \tag{34}$$

$$\boldsymbol{A}_{1\aleph} = \left(\mathbf{1} - \boldsymbol{d}_{0\aleph} - \boldsymbol{\lambda}_\aleph\right)\left(\boldsymbol{\varepsilon}_{f\aleph} - \boldsymbol{\varepsilon}_{0\aleph}\right)^{-\boldsymbol{B}_{1\aleph}} \tag{35}$$

$$\boldsymbol{B}_{2\aleph} = \frac{\bar{\boldsymbol{\sigma}}_{f\aleph} - \boldsymbol{\varepsilon}_{f\aleph}\bar{\boldsymbol{\sigma}}'_{f\aleph}}{\bar{\boldsymbol{\sigma}}_{f\aleph}} \tag{36}$$

$$\boldsymbol{\lambda}_\aleph = \frac{\boldsymbol{\sigma}_{f\aleph}}{\bar{\boldsymbol{\sigma}}_{f\aleph}} \tag{37}$$

where $\bar{\sigma}'_{f\aleph}$ is the derivative of the effective stress with respect to the peak strain $\varepsilon_{f\aleph}$. Fig. 1 illustrates the evolution curves of the effective/nominal stress and damage variable of the proposed model under uniaxial loading cases (tension and compression).

3.5 Consistent tangent stiffness

At each time step, the nominal stress increment $d\boldsymbol{\sigma}$ within iteration $i \to i+1$ is

$$\boldsymbol{d\sigma} = \left(\mathbf{1} - {}_i\bar{\boldsymbol{d}}\right)\boldsymbol{d\bar{\sigma}} - {}_i\bar{\boldsymbol{\sigma}}\boldsymbol{d\bar{d}} \tag{38}$$

with

$$\begin{aligned}\boldsymbol{d\bar{\sigma}} &= \boldsymbol{D}^e : \left(\boldsymbol{d\varepsilon} - \boldsymbol{d\varepsilon}^p\right) \\ &= \boldsymbol{D}^e : \boldsymbol{d\varepsilon} - \Delta\boldsymbol{\lambda}^p \boldsymbol{D}^e : \frac{\partial \boldsymbol{m}}{\partial \bar{\boldsymbol{\sigma}}} : \boldsymbol{d\bar{\sigma}} - \boldsymbol{D}^e : \boldsymbol{m}\boldsymbol{d\lambda}^p\end{aligned} \tag{39}$$

This equation can be rewritten as

$$\boldsymbol{d\bar{\sigma}} = \boldsymbol{D}^a : \boldsymbol{d\varepsilon} - \boldsymbol{D}^a : \boldsymbol{m}\boldsymbol{d\lambda}^p \tag{40}$$

where

$$\boldsymbol{D}^a = \left[\left(\boldsymbol{D}^e\right)^{-1} + \Delta\boldsymbol{\lambda}^p \frac{\partial \boldsymbol{m}}{\partial \bar{\boldsymbol{\sigma}}}\right]^{-1} \tag{41}$$

The yield function of concrete should satisfy the continuity requirement.

$$\boldsymbol{dF} = \frac{\partial \boldsymbol{F}}{\partial \bar{\boldsymbol{\sigma}}} : \boldsymbol{d\bar{\sigma}} + \frac{\partial \boldsymbol{F}}{\partial \boldsymbol{\kappa}} : \boldsymbol{d\kappa} = \mathbf{0} \tag{42}$$

where the increment in the internal variables can be calculated as follows

$$\boldsymbol{d\kappa} = \boldsymbol{h}\boldsymbol{d\lambda}^p + \Delta\boldsymbol{\lambda}^p \frac{\partial \boldsymbol{h}}{\partial \bar{\boldsymbol{\sigma}}} : \boldsymbol{d\bar{\sigma}} \tag{43}$$

The substitution of Eqs. (40) and (43) into Eq. (42) leads to an expression of $d\lambda^{\mathrm{p}}$ in terms of $d\boldsymbol{\varepsilon}$

$$\boldsymbol{d\lambda}^p = \frac{\left(\frac{\partial \boldsymbol{F}}{\partial \bar{\boldsymbol{\sigma}}} + \Delta\boldsymbol{\lambda}^p \frac{\partial \boldsymbol{F}}{\partial \boldsymbol{\kappa}} : \frac{\partial \boldsymbol{h}}{\partial \bar{\boldsymbol{\sigma}}}\right)\boldsymbol{D}^a}{\boldsymbol{H}_a + \left(\frac{\partial \boldsymbol{F}}{\partial \bar{\boldsymbol{\sigma}}} + \Delta\boldsymbol{\lambda}^p \frac{\partial \boldsymbol{F}}{\partial \boldsymbol{\kappa}} : \frac{\partial \boldsymbol{h}}{\partial \bar{\boldsymbol{\sigma}}}\right) : \boldsymbol{D}^a : \boldsymbol{m}} : \boldsymbol{d\varepsilon} \tag{44}$$

where $H_a = -\frac{\partial F}{\partial \boldsymbol{\kappa}} : \mathbf{h}$.

In Eq. (44), the effective stress increment $d\bar{\boldsymbol{\sigma}}$ can be expressed in terms of $d\boldsymbol{\varepsilon}$.

$$\begin{aligned}&\boldsymbol{d\bar{\sigma}} \\ &= \left(\boldsymbol{D}^a - \frac{\boldsymbol{D}^a : \boldsymbol{m} \otimes \left(\frac{\partial \boldsymbol{F}}{\partial \bar{\boldsymbol{\sigma}}} + \Delta\boldsymbol{\lambda}^p \frac{\partial \boldsymbol{F}}{\partial \boldsymbol{\kappa}} : \frac{\partial \boldsymbol{h}}{\partial \bar{\boldsymbol{\sigma}}}\right)\boldsymbol{D}^a}{\boldsymbol{H}_a + \left(\frac{\partial \boldsymbol{F}}{\partial \bar{\boldsymbol{\sigma}}} + \Delta\boldsymbol{\lambda}^p \frac{\partial \boldsymbol{F}}{\partial \boldsymbol{\kappa}} : \frac{\partial \boldsymbol{h}}{\partial \bar{\boldsymbol{\sigma}}}\right) : \boldsymbol{D}^a : \boldsymbol{m}}\right) : \boldsymbol{d\varepsilon} \\ &= \boldsymbol{D}^{ep}_{\bar{\boldsymbol{\sigma}}} : \boldsymbol{d\varepsilon}\end{aligned} \tag{45}$$

When $d\lambda^{\mathrm{p}}$ and $d\bar{\boldsymbol{\sigma}}$ are simultaneously substituted into Eq. (43), the increment in internal variable $d\boldsymbol{\kappa}$ can be formulated in terms of strain increment $d\boldsymbol{\varepsilon}$ as follows

$$\begin{aligned}\boldsymbol{d\kappa} = \Bigg(&\boldsymbol{h} \otimes \frac{\left(\frac{\partial \boldsymbol{F}}{\partial \bar{\boldsymbol{\sigma}}} + \Delta\boldsymbol{\lambda}^p \frac{\partial \boldsymbol{F}}{\partial \boldsymbol{\kappa}} : \frac{\partial \boldsymbol{h}}{\partial \bar{\boldsymbol{\sigma}}}\right)\boldsymbol{D}^a}{\boldsymbol{H}_a + \left(\frac{\partial \boldsymbol{F}}{\partial \bar{\boldsymbol{\sigma}}} + \Delta\boldsymbol{\lambda}^p \frac{\partial \boldsymbol{F}}{\partial \boldsymbol{\kappa}} : \frac{\partial \boldsymbol{h}}{\partial \bar{\boldsymbol{\sigma}}}\right) : \boldsymbol{D}^a : \boldsymbol{m}} \\ &+ \Delta\boldsymbol{\lambda}^p \frac{\partial \boldsymbol{h}}{\partial \bar{\boldsymbol{\sigma}}} : \boldsymbol{D}^{ep}_{\bar{\boldsymbol{\sigma}}}\Bigg) : \boldsymbol{d\varepsilon} = \boldsymbol{D}^{ep}_{\boldsymbol{\kappa}} : \boldsymbol{d\varepsilon}\end{aligned} \tag{46}$$

The damage increment $d\bar{d}$ of concrete can be obtained by using

$$\boldsymbol{d\bar{d}} = \frac{\boldsymbol{d\bar{d}}}{\boldsymbol{d\bar{\kappa}}} \boldsymbol{R}_{\bar{\kappa}} \boldsymbol{d\bar{\kappa}} \tag{47}$$

where $\mathbf{R}_{\bar{\kappa}}$ is the interpolation function for $\bar{\boldsymbol{\kappa}}$.

The substitution of Eq.(45) and (47) into Eq.(40) to obtain the expression of the increment in nominal stress for the gradient-enhanced damage-plasticity model yields the following equation

$$\boldsymbol{d\sigma} = \left(\mathbf{1} - {}_i\bar{\boldsymbol{d}}\right)\boldsymbol{D}^{ep}_{\bar{\boldsymbol{\sigma}}} : \boldsymbol{d\varepsilon} - {}_i\bar{\boldsymbol{\sigma}} \frac{\boldsymbol{d\bar{d}}}{\boldsymbol{d\bar{\kappa}}} \boldsymbol{d\bar{\kappa}} \tag{48}$$

4. Implicit gradient formulation of internal variables

Jirasek (1998) highlighted that the nonlocal variables must be selected carefully for strain-softening materials, which account for plasticity. Otherwise, stress locking may occur in numerical solutions. Generally, equivalent strain, plastic-hardening variable or damage can be selected as nonlocal variables. In this study, $\bar{\boldsymbol{\kappa}} = (\bar{\kappa}_t, \bar{\kappa}_c)^{\mathrm{T}}$ is defined as follows

$$\bar{\boldsymbol{\kappa}}(\boldsymbol{x}) = \frac{\int_{\Omega} \boldsymbol{\psi}(\boldsymbol{x},\boldsymbol{y}) \cdot \boldsymbol{\kappa}(\boldsymbol{y}) d\boldsymbol{\Omega}}{\int_{\Omega} \boldsymbol{\psi}(\boldsymbol{x},\boldsymbol{y})\, d\boldsymbol{\Omega}} \tag{49}$$

For sufficiently smooth $\kappa_{\aleph}(\cdot)$ -fields, the integral relation in Eq.(49) can be rewritten in terms of gradients of $\kappa_{\aleph}(\cdot)$ by expanding $\kappa_{\aleph}(\mathbf{y})$ into a Taylor series (e.g., Bazant *et al*. 1984; Peerlings *et al*. 1996a; Peerlings *et al*. 1996b)

$$\begin{aligned}\boldsymbol{\kappa}_{\aleph}(\mathbf{y}) = \boldsymbol{\kappa}_{\aleph}(\mathbf{x}) &+ \frac{\partial \boldsymbol{\kappa}_{\aleph}}{\partial \boldsymbol{x}_i}(\boldsymbol{y}_i - \boldsymbol{x}_i) \\ &+ \frac{1}{2!}\frac{\partial^2 \boldsymbol{\kappa}_{\aleph}}{\partial \boldsymbol{x}_i \partial \boldsymbol{x}_j}(\boldsymbol{y}_i - \boldsymbol{x}_i)(\boldsymbol{y}_j - \boldsymbol{x}_j) \\ &+ \frac{1}{3!}\frac{\partial^3 \boldsymbol{\kappa}_{\aleph}}{\partial \boldsymbol{x}_i \partial \boldsymbol{x}_j \partial \boldsymbol{x}_k}(\boldsymbol{y}_i - \boldsymbol{x}_i)(\boldsymbol{y}_j - \boldsymbol{x}_j)(\boldsymbol{y}_k - \boldsymbol{x}_k) \\ &+ \frac{1}{4!}\frac{\partial^4 \boldsymbol{\kappa}_{\aleph}}{\partial \boldsymbol{x}_i \partial \boldsymbol{x}_j \partial \boldsymbol{x}_k \partial \boldsymbol{x}_l}(\boldsymbol{y}_i - \boldsymbol{x}_i)(\boldsymbol{y}_j - \boldsymbol{x}_j) \\ &(\boldsymbol{y}_k - \boldsymbol{x}_k)(\boldsymbol{y}_l - \boldsymbol{x}_l) + \cdots\cdots\end{aligned} \tag{50}$$

where the indices i, j, k, and l satisfy Einstein's summation convention. The substitution of Eq.(50) into Eq.(49) and evaluation of the integral within the space range result in the following equation

$$\bar{\boldsymbol{\kappa}}_{\aleph}(\boldsymbol{x}) = \boldsymbol{\kappa}_{\aleph}(\boldsymbol{x}) + \boldsymbol{c}_2 \cdot \boldsymbol{\nabla}^2 \boldsymbol{\kappa}_{\aleph}(\boldsymbol{x}) + \boldsymbol{c}_4 \cdot \boldsymbol{\nabla}^4 \boldsymbol{\kappa}_{\aleph}(\boldsymbol{x}) + \cdots \tag{51}$$

where ∇^{2n} is the Laplace operator, which is defined as $\nabla^2 = \sum_i \partial^2/\partial x_i^2$, and $\nabla^{2n} = (\nabla^2)^n$; $c_{2n}(n = 1,2,\cdots)$ are the gradient coefficients that depend on the form of weighting function $\psi(\mathbf{x},\mathbf{y})$ and include the material characteristic length l_{ch}.

$c = c_2$ is denoted, and neglecting the derivative terms of an order higher than two on the right side of Eq.(51) result in the second-order explicit gradient formulation for $\bar{\kappa}_{\aleph}(\mathbf{x})$.

$$\bar{\boldsymbol{\kappa}}_{\aleph}(\boldsymbol{x}) = \boldsymbol{\kappa}_{\aleph}(\boldsymbol{x}) + \boldsymbol{c} \cdot \boldsymbol{\nabla}^2 \boldsymbol{\kappa}_{\aleph}(\boldsymbol{x}) \tag{52}$$

The material characteristic length l_{ch} is considered in the gradient coefficient c. However, $\kappa(\mathbf{x})$ and its second-order derivative $\nabla^2\kappa_{\aleph}(\mathbf{x})$ are mathematically local quantities; thus, $\bar{\kappa}(\mathbf{x})$ calculated using Eq.(52) is local, thereby indicating that an explicit gradient approximation is only weakly nonlocal (interactions limited to an infinitesimal neighborhood). The weak nonlocal character of an explicit gradient formulation can be improved by further mathematical treatments in Eq.(51), such that the second-order implicit gradient formulation for $\bar{\kappa}_{\aleph}(\mathbf{x})$ can be derived as follows (e.g., Engelen *et al*. 2003)

$$\bar{\boldsymbol{\kappa}}_{\aleph}(\boldsymbol{x}) - \boldsymbol{c} \cdot \boldsymbol{\nabla}^2 \bar{\boldsymbol{\kappa}}_{\aleph}(\boldsymbol{x}) = \boldsymbol{\kappa}_{\aleph}(\boldsymbol{x}) \tag{53}$$

Here, the second-order implicit gradient formulation of $\bar{\boldsymbol{\kappa}}$ is easily obtained as follows

$$\bar{\boldsymbol{\kappa}} - \boldsymbol{c} \cdot \boldsymbol{\nabla}^2 \bar{\boldsymbol{\kappa}} = \boldsymbol{\kappa} \;\Leftrightarrow\; \begin{cases} \bar{\boldsymbol{\kappa}}_t - \boldsymbol{c} \cdot \boldsymbol{\nabla}^2 \bar{\boldsymbol{\kappa}}_t = \boldsymbol{\kappa}_t \\ \bar{\boldsymbol{\kappa}}_c - \boldsymbol{c} \cdot \boldsymbol{\nabla}^2 \bar{\boldsymbol{\kappa}}_c = \boldsymbol{\kappa}_c \end{cases} \tag{54}$$

If nonlocal internal variables $\bar{\boldsymbol{\kappa}}$ only affect the evolution of concrete damage, then the plastic hardening of concrete remains governed by the local internal variable $\boldsymbol{\kappa}$. Therefore, the governing equations of the gradient-enhanced damage-plasticity model can be summarized as follows

$$\begin{cases} \boldsymbol{\varepsilon} = \boldsymbol{\varepsilon}^e + \boldsymbol{\varepsilon}^p \\ \boldsymbol{\sigma} = (\mathbf{1} - \bar{\boldsymbol{d}})\bar{\boldsymbol{\sigma}} \\ \bar{\boldsymbol{d}} = \boldsymbol{d}(\bar{\boldsymbol{\kappa}}) \\ \dot{\boldsymbol{\varepsilon}}^p = \dot{\boldsymbol{\lambda}}^p \boldsymbol{m}(\bar{\boldsymbol{\sigma}}, \boldsymbol{\kappa}) = \dot{\boldsymbol{\lambda}}^p \dfrac{\partial \boldsymbol{\Phi}(\bar{\boldsymbol{\sigma}}, \boldsymbol{\kappa})}{\partial \bar{\boldsymbol{\sigma}}} \\ \dot{\boldsymbol{\kappa}} = \dot{\boldsymbol{\lambda}}^p \boldsymbol{h}(\bar{\boldsymbol{\sigma}}, \boldsymbol{\kappa}) \\ \dot{\boldsymbol{\lambda}}^p \geq \mathbf{0},\;\; \boldsymbol{F}(\bar{\boldsymbol{\sigma}}, \boldsymbol{\kappa}) \leq \mathbf{0} \;\; \textbf{with} \;\; \dot{\boldsymbol{\lambda}}^p \boldsymbol{F} = \mathbf{0} \end{cases} \tag{55}$$

where $\bar{d}$ is the nonlocal damage.

The averaging partial differential Eq. (53) can be solved by applying an additional natural boundary condition to $\bar{\kappa}_{\aleph}(\mathbf{x})$, as follows

$$\boldsymbol{\nabla} \bar{\boldsymbol{\kappa}}_{\aleph}(\boldsymbol{x}) \cdot \boldsymbol{n} = \mathbf{0}, \textbf{for}\; \boldsymbol{x} \subset \boldsymbol{\Gamma} = \partial \boldsymbol{\Omega} \tag{56}$$

where $\mathbf{n}$ is the outward normal unit vector to the boundary Γ of the analysis domain. A coincident regularization effect of $\kappa_{\aleph}(\mathbf{x})$ and $\bar{\kappa}_{\aleph}(\mathbf{x})$ can be ensured by relating Eq. (54) to Eq. (56).

$$\int_{\Omega} \bar{\boldsymbol{\kappa}}_{\aleph}(\boldsymbol{x})\, d\boldsymbol{\Omega} = \int_{\Omega} \boldsymbol{\kappa}_{\aleph}(\boldsymbol{x})\, d\boldsymbol{\Omega} \tag{57}$$

The nonlocal weight function is selected as Green's distribution function.

$$\boldsymbol{\psi}(\boldsymbol{x},\boldsymbol{y}) = \frac{\mathbf{1}}{4\boldsymbol{\pi}|\boldsymbol{r}|\boldsymbol{l}_{ch}^2} \boldsymbol{exp}\left(-\frac{|\boldsymbol{r}|}{\boldsymbol{l}_{ch}}\right) \tag{58}$$

where $r = \|\mathbf{x} - \mathbf{y}\|$ is the distance between points $\mathbf{x}$ and $\mathbf{y}$ and can be obtained as follows (e.g., Engelen *et al*. 2003)

$$\boldsymbol{c} = \boldsymbol{l}_{ch}^2 \tag{59}$$

Fig. 2 depicts the distribution curves of the nonlocal damage variable $\bar{d}_{\aleph}$ that corresponds to different values of c in 1D. When $c = 0$, the nonlocal damage variable $\bar{d}_{\aleph}$

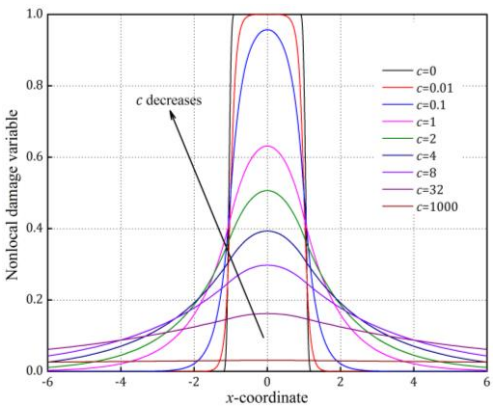

Fig. 2 Distribution curves of $\bar{d}_{\aleph}$, which corresponds to the different values of c

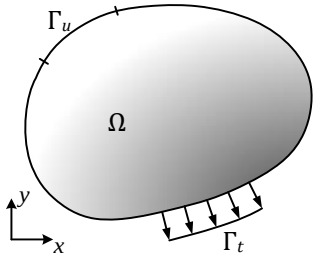

Fig. 3 Domain Ω of IGA

completely degrades to the local damage variable $d_{\aleph}$. The localized distribution property of $\bar{d}_{\aleph}$ along the x-axis becomes less obvious than usual given the increase in the value of c. When c is used as a relatively high value, $\bar{d}_{\aleph}$ shows a completely uniform distribution along the x-axis.

5. Numerical framework

5.1 Weak form and discretization

The domain Ω with boundary $\Gamma = \partial\Omega$ must be considered, as demonstrated in Fig. 3. The equilibrium equation can be expressed as follows

$$\boldsymbol{\nabla_u \cdot \sigma + \bar{f} = 0, \text{in } \Omega} \tag{60}$$

where ∇_u is the differential operator, and $\bar{\mathbf{f}}$ is the body force.

The boundary is partitioned into two sets, namely, Γ_u and Γ_t, with displacements prescribed on Γ_u and traction $\bar{\mathbf{t}}$ prescribed on Γ_t; thus

$$\boldsymbol{u = \bar{u}, \text{on } \Gamma_u} \tag{61}$$

$$\boldsymbol{\sigma \cdot n = \bar{t}, \text{on } \Gamma_t} \tag{62}$$

The test functions of the displacement field $\mathbf{u}$ and nonlocal internal variables $\bar{\boldsymbol{\kappa}}$ must be denoted as $\boldsymbol{\omega}_u$ and $\boldsymbol{\omega}_{\bar{\kappa}}$, correspondingly; Eq. (60) and Eq. (54) can be formulated in an integral form as follows

$$\int_{\Omega} \boldsymbol{\omega}_u^T \cdot (\boldsymbol{\nabla}_u \cdot \boldsymbol{\sigma} + \boldsymbol{f}) d\boldsymbol{\Omega} = \mathbf{0} \tag{63}$$

$$\int_{\Omega} \boldsymbol{\omega}_{\bar{\kappa}}^{\mathbf{T}} \cdot (\bar{\boldsymbol{\kappa}} - \boldsymbol{c} \cdot \boldsymbol{\nabla}^2 \bar{\boldsymbol{\kappa}}) \mathbf{d\Omega} = \int_{\Omega} \boldsymbol{\omega}_{\bar{\kappa}}^{\mathbf{T}} \cdot \boldsymbol{\kappa} \mathbf{d\Omega} \tag{64}$$

where superscript T indicates the transpose.

An integration by parts followed by applying a divergence theorem with the associated boundary conditions yield the following equation

$$\int_{\Omega} (\boldsymbol{\nabla}_u \boldsymbol{\omega}_u)^T \boldsymbol{\sigma} d\boldsymbol{\Omega} = \int_{\Omega} \boldsymbol{\omega}_u^T \boldsymbol{f} d\boldsymbol{\Omega} + \int_{\Gamma_\sigma} \boldsymbol{\omega}_u^T \boldsymbol{t} d\boldsymbol{\Gamma}_\sigma \tag{65}$$

$$\int_{\Omega} \boldsymbol{\omega}_{\bar{\kappa}}^{\mathbf{T}} \bar{\boldsymbol{\kappa}} \, \mathbf{d\Omega} + \int_{\Omega} \boldsymbol{\nabla} \boldsymbol{\omega}_{\bar{\kappa}}^{\mathbf{T}} \boldsymbol{c} \boldsymbol{\nabla} \bar{\boldsymbol{\kappa}} \, \mathbf{d\Omega} = \int_{\Omega} \boldsymbol{\omega}_{\bar{\kappa}}^{\mathbf{T}} \boldsymbol{\kappa} \, \mathbf{d\Omega} \tag{66}$$

If Ω consists of ne NURBS elements, then $\boldsymbol{\omega}_u$ and $\boldsymbol{\omega}_{\bar{\kappa}}$ can be calculated as follows

$$\boldsymbol{\omega_u = R_u \omega_{u,N}} \tag{67}$$

$$\boldsymbol{\omega_{\bar{\kappa}} = R_{\bar{\kappa}} \omega_{\bar{\kappa},N}} \tag{68}$$

where $\boldsymbol{\omega}_{u,N}$ and $\boldsymbol{\omega}_{\bar{\kappa},N}$ are the weight functions of displacement $\mathbf{u}$ and nonlocal internal variables $\bar{\boldsymbol{\kappa}}$ for the control points of the NURBS element, respectively. $\mathbf{R}_u$ and $\mathbf{R}_{\bar{\kappa}}$ are the interpolation function matrices expressed as follows

$$\boldsymbol{R_u} = \begin{bmatrix} \boldsymbol{R_1^p} & \mathbf{0} & \mathbf{0} & & \boldsymbol{R_{npt}^p} & \mathbf{0} & \mathbf{0} \\ \mathbf{0} & \boldsymbol{R_1^p} & \mathbf{0} & \cdots\cdots & \mathbf{0} & \boldsymbol{R_{npt}^p} & \mathbf{0} \\ \mathbf{0} & \mathbf{0} & \boldsymbol{R_1^p} & & \mathbf{0} & \mathbf{0} & \boldsymbol{R_{npt}^p} \end{bmatrix} \tag{69}$$

$$\mathbf{R}_{\bar{\kappa}} = \begin{bmatrix} \boldsymbol{R_1^p} & & \cdots\cdots & \boldsymbol{R_{npt}^p} & \\ & \boldsymbol{R_1^p} & & & \boldsymbol{R_{npt}^p} \end{bmatrix} \tag{70}$$

where $R_{ipt}^p = R_{ipt}^p(\tilde{\xi}, \tilde{\eta})$ is the pth-order NURBS basis function of control point ipt.

The spatial derivatives of $\boldsymbol{\omega}_u$ and $\boldsymbol{\omega}_{\bar{\kappa}}$ are obtained by using the following equation

$$\boldsymbol{\nabla_u \omega_u = \nabla_u R_u \omega_{u,N} = B_u \omega_{u,N}} \tag{71}$$

$$\boldsymbol{\nabla \omega_{\bar{\kappa}} = \nabla R_{\bar{\kappa}} \omega_{\bar{\kappa},N} = B_{\bar{\kappa}} \omega_{\bar{\kappa},N}} \tag{72}$$

where $\mathbf{B}_u = \nabla_u \mathbf{R}_u$, and $\mathbf{B}_{\bar{\kappa}} = \nabla \mathbf{R}_{\bar{\kappa}}$.

The displacement and nonlocal internal variables are discretized with the NURBS basis functions.

$$\boldsymbol{u = R_u u_N} \tag{73}$$

$$\boldsymbol{\bar{\kappa} = R_{\bar{\kappa}} \bar{\kappa}_N} \tag{74}$$

Their gradients are obtained through the following equation

$$\boldsymbol{\varepsilon = \nabla_u R_u u_N = B_u u_N} \tag{75}$$

$$\boldsymbol{\nabla \bar{\kappa} = \nabla R_{\bar{\kappa}} \bar{\kappa}_N = B_{\bar{\kappa}} \bar{\kappa}_N} \tag{76}$$

The substitution of Eqs. (71) and (72) into Eqs. (65) and (66), correspondingly, yields the following equation

$$\int_{\Omega} \boldsymbol{B_u^T \sigma d\Omega} = \int_{\Omega} \boldsymbol{R_u^T f d\Omega} + \int_{\Gamma} \boldsymbol{R_u^T t d\Gamma} \tag{77}$$

$$\int_{\Omega} (\boldsymbol{R_{\bar{\kappa}}^T R_{\bar{\kappa}} + B_{\bar{\kappa}}^T c B_{\bar{\kappa}}}) \boldsymbol{\bar{\kappa}_N} \, \boldsymbol{d\Omega} = \int_{\Omega} \boldsymbol{R_{\bar{\kappa}}^T \kappa d\Omega} \tag{78}$$

The Newton method for a linearized system of equations is used, in which the following fields are updated by

$$\boldsymbol{{}_{i+1}u_N = {}_i u_N + du_N} \tag{79}$$

$$\boldsymbol{{}_{i+1}\bar{\kappa}_N = {}_i \bar{\kappa}_N + d\bar{\kappa}_N} \tag{80}$$

$$\boldsymbol{{}_{i+1}\sigma = {}_i \sigma + d\sigma} \tag{81}$$

where $\mathbf{u}_N$ and $\bar{\boldsymbol{\kappa}}_N$ are the vectors of displacement and nonlocal internal variables at the control points, respectively, with $d\mathbf{u}_N$ and $d\bar{\boldsymbol{\kappa}}_N$ being the corresponding increments. Moreover, the iteration index is denoted by i. Thus, Eq. (77) and Eq. (78) can be rewritten as follows

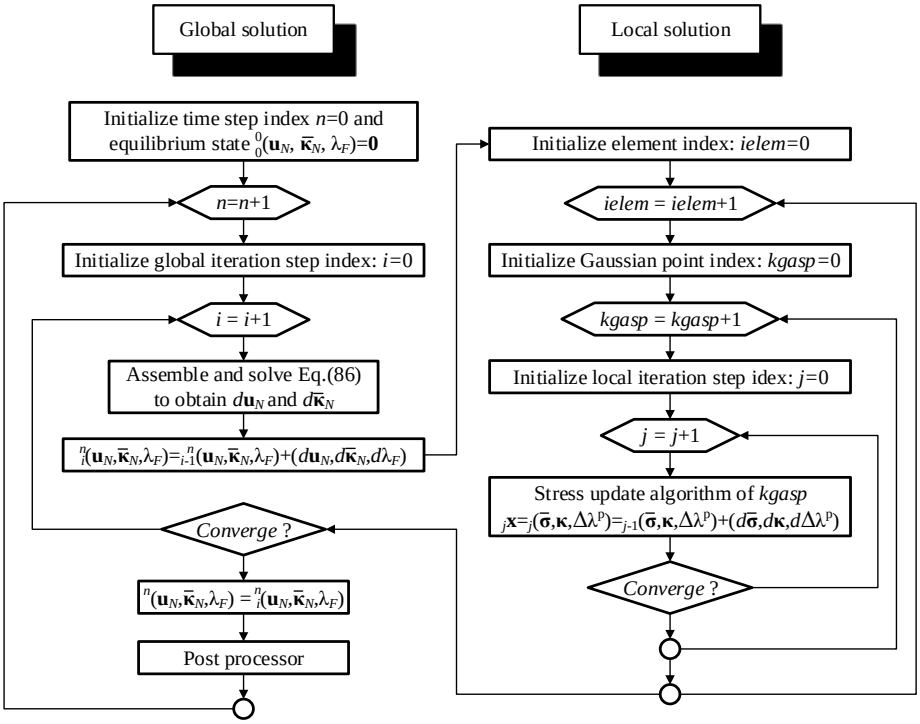

Fig. 4 Flowchart of procedure

$$\int_{\Omega} \boldsymbol{B}_{\boldsymbol{u}}^{\boldsymbol{T}} \cdot {}_{i+1}\boldsymbol{\sigma}\, d\boldsymbol{\Omega} = \int_{\Omega} \boldsymbol{B}_{\boldsymbol{u}}^{\boldsymbol{T}} \left({}_{i+1}\boldsymbol{\sigma} + d\boldsymbol{\sigma}\right) d\boldsymbol{\Omega} = \int_{\Omega} \boldsymbol{R}_{\boldsymbol{u}}^{\boldsymbol{T}} \cdot {}_{i+1}\boldsymbol{f}\, d\boldsymbol{\Omega} + \int_{\Gamma} \boldsymbol{R}_{\boldsymbol{u}}^{\boldsymbol{T}} \cdot {}_{i+1}\boldsymbol{t}\, d\boldsymbol{\Gamma} \tag{82}$$

$$\int_{\Omega} \left(\boldsymbol{R}_{\bar{\boldsymbol{\kappa}}}^{\boldsymbol{T}} \boldsymbol{R}_{\bar{\boldsymbol{\kappa}}} + \boldsymbol{B}_{\bar{\boldsymbol{\kappa}}}^{\boldsymbol{T}} \boldsymbol{c} \boldsymbol{B}_{\bar{\boldsymbol{\kappa}}}\right) \left({}_{i}\bar{\boldsymbol{\kappa}}_{\boldsymbol{N}} + d\bar{\boldsymbol{\kappa}}_{\boldsymbol{N}} \right) d\boldsymbol{\Omega} = \int_{\Omega} \boldsymbol{R}_{\bar{\boldsymbol{\kappa}}}^{\boldsymbol{T}} \left({}_{i}\boldsymbol{\kappa} + d\boldsymbol{\kappa} \right) d\boldsymbol{\Omega} \tag{83}$$

The substitution of Eq.(48) into Eq.(82) leads to

$$\int_{\Omega} \mathbf{B}_{\boldsymbol{u}}^{\mathbf{T}} \left(\mathbf{1} - {}_{i}\bar{\boldsymbol{d}}\right) \mathbf{D}_{\bar{\boldsymbol{\sigma}}}^{\mathbf{ep}} \mathbf{B}_{\boldsymbol{u}} d\boldsymbol{\Omega} \cdot d\mathbf{u}_{\boldsymbol{N}} - \int_{\Omega} \mathbf{B}_{\boldsymbol{u}}^{\mathbf{T}} \, {}_{i}\bar{\boldsymbol{\sigma}} \frac{\mathbf{d}\bar{\boldsymbol{d}}}{\mathbf{d}\bar{\boldsymbol{\kappa}}} \mathbf{R}_{\bar{\boldsymbol{\kappa}}} d\boldsymbol{\Omega} \cdot d\bar{\boldsymbol{\kappa}}_{\boldsymbol{N}} = \int_{\Omega} \mathbf{R}_{\boldsymbol{u}}^{\mathbf{T}} \cdot {}_{i+1}\mathbf{f} d\boldsymbol{\Omega} + \int_{\Gamma} \mathbf{R}_{\boldsymbol{u}}^{\mathbf{T}} \cdot {}_{i+1}\mathbf{t} d\boldsymbol{\Gamma} - \int_{\Omega} \mathbf{B}_{\boldsymbol{u}}^{\mathbf{T}} \cdot \, {}_{i}\boldsymbol{\sigma} d\boldsymbol{\Omega} \tag{84}$$

The substitution of Eq.(46) into Eq.(83) can obtain

$$-\int_{\Omega} \mathbf{R}_{\bar{\boldsymbol{\kappa}}}^{\mathbf{T}} \mathbf{D}_{\boldsymbol{\kappa}}^{\mathbf{ep}} \mathbf{B}_{\boldsymbol{u}} d\boldsymbol{\Omega} \cdot d\mathbf{u}_{\boldsymbol{N}} + \int_{\Omega} \left(\mathbf{R}_{\bar{\boldsymbol{\kappa}}}^{\mathbf{T}} \mathbf{R}_{\bar{\boldsymbol{\kappa}}} + \mathbf{R}_{\bar{\boldsymbol{\kappa}}}^{\mathbf{T}} \boldsymbol{c} \mathbf{B}_{\bar{\boldsymbol{\kappa}}}\right) d\boldsymbol{\Omega} \cdot d\bar{\boldsymbol{\kappa}}_{\boldsymbol{N}} = \int_{\Omega} \boldsymbol{R}_{\bar{\boldsymbol{\kappa}}}^{\boldsymbol{T}} \cdot \, {}_{i}\boldsymbol{\kappa} d\boldsymbol{\Omega} - \int_{\Omega} \left(\boldsymbol{R}_{\bar{\boldsymbol{\kappa}}}^{\boldsymbol{T}} \boldsymbol{R}_{\bar{\boldsymbol{\kappa}}} + \boldsymbol{B}_{\bar{\boldsymbol{\kappa}}}^{\boldsymbol{T}} \boldsymbol{c} \boldsymbol{B}_{\bar{\boldsymbol{\kappa}}}\right) \cdot \, {}_{i}\bar{\boldsymbol{\kappa}}_{\boldsymbol{N}} d\boldsymbol{\Omega} \tag{85}$$

By combining Eq.(84) and Eq.(85) in a matrix form, the following discrete system of equations is obtained.

$$\begin{pmatrix} {}_{i+1}\mathbf{K}_{\boldsymbol{uu}} & {}_{i+1}\mathbf{K}_{\boldsymbol{u}\bar{\boldsymbol{\kappa}}} \\ {}_{i+1}\mathbf{K}_{\bar{\boldsymbol{\kappa}}\boldsymbol{u}} & {}_{i+1}\mathbf{K}_{\bar{\boldsymbol{\kappa}}\bar{\boldsymbol{\kappa}}} \end{pmatrix} \begin{pmatrix} d\mathbf{u}_{\boldsymbol{N}} \\ d\bar{\boldsymbol{\kappa}}_{\boldsymbol{N}} \end{pmatrix} = \begin{pmatrix} {}_{i+1}\mathbf{f}_{\boldsymbol{u}}^{\mathbf{ext}} \\ {}_{i+1}\mathbf{f}_{\bar{\boldsymbol{\kappa}}}^{\mathbf{ext}} \end{pmatrix} - \begin{pmatrix} {}_{i+1}\mathbf{f}_{\boldsymbol{u}}^{\mathbf{int}} \\ {}_{i+1}\mathbf{f}_{\bar{\boldsymbol{\kappa}}}^{\mathbf{int}} \end{pmatrix} \tag{86}$$

where submatrices are defined as follows

$$\begin{aligned}
{}_{i+1}\boldsymbol{K}_{\boldsymbol{uu}} &= \int_{\Omega} \boldsymbol{B}_{\boldsymbol{u}}^{\boldsymbol{T}} \left(\mathbf{1} - {}_{i}\bar{\boldsymbol{d}}\right) \boldsymbol{D}_{\bar{\boldsymbol{\sigma}}}^{\boldsymbol{ep}} \boldsymbol{B}_{\boldsymbol{u}} d\boldsymbol{\Omega} \\
{}_{i+1}\mathbf{K}_{\boldsymbol{u}\bar{\boldsymbol{\kappa}}} &= -\int_{\Omega} \mathbf{B}_{\boldsymbol{u}}^{\mathbf{T}} \, {}_{i}\bar{\boldsymbol{\sigma}} \frac{\mathbf{d}\bar{\boldsymbol{d}}}{\mathbf{d}\bar{\boldsymbol{\kappa}}} \mathbf{R}_{\bar{\boldsymbol{\kappa}}} d\boldsymbol{\Omega} \\
{}_{i+1}\mathbf{K}_{\bar{\boldsymbol{\kappa}}\boldsymbol{u}} &= -\int_{\Omega} \mathbf{R}_{\bar{\boldsymbol{\kappa}}}^{\mathbf{T}} \mathbf{D}_{\boldsymbol{\kappa}}^{\mathbf{ep}} \mathbf{B}_{\boldsymbol{u}} d\boldsymbol{\Omega} \cdot d\mathbf{u}_{\boldsymbol{N}} \\
{}_{i+1}\mathbf{K}_{\bar{\boldsymbol{\kappa}}\bar{\boldsymbol{\kappa}}} &= \int_{\Omega} \left(\mathbf{R}_{\bar{\boldsymbol{\kappa}}}^{\mathbf{T}} \mathbf{R}_{\bar{\boldsymbol{\kappa}}} + \mathbf{B}_{\bar{\boldsymbol{\kappa}}}^{\mathbf{T}} \boldsymbol{c} \mathbf{B}_{\bar{\boldsymbol{\kappa}}}\right) d\boldsymbol{\Omega} \\
{}_{i+1}\mathbf{f}_{\boldsymbol{u}}^{\mathbf{ext}} &= \int_{\Omega} \mathbf{R}_{\boldsymbol{u}}^{\mathbf{T}} \cdot {}_{i+1}\mathbf{f} d\boldsymbol{\Omega} + \int_{\Gamma} \mathbf{R}_{\boldsymbol{u}}^{\mathbf{T}} \cdot {}_{i+1}\mathbf{t} d\boldsymbol{\Gamma} \\
{}_{i+1}\mathbf{f}_{\boldsymbol{u}}^{\mathbf{int}} &= \int_{\Omega} \mathbf{B}_{\boldsymbol{u}}^{\mathbf{T}} \cdot \, {}_{i}\boldsymbol{\sigma} d\boldsymbol{\Omega} \\
{}_{i+1}\mathbf{f}_{\bar{\boldsymbol{\kappa}}}^{\mathbf{ext}} &= \mathbf{0} \\
{}_{i+1}\mathbf{f}_{\bar{\boldsymbol{\kappa}}}^{\mathbf{int}} &= \int_{\Omega} \left(\mathbf{R}_{\bar{\boldsymbol{\kappa}}}^{\mathbf{T}} \mathbf{R}_{\bar{\boldsymbol{\kappa}}} + \mathbf{B}_{\bar{\boldsymbol{\kappa}}}^{\mathbf{T}} \boldsymbol{c} \mathbf{B}_{\bar{\boldsymbol{\kappa}}}\right) \cdot \, {}_{i}\bar{\boldsymbol{\kappa}}_{\boldsymbol{N}} d\boldsymbol{\Omega} - \int_{\Omega} \mathbf{R}_{\bar{\boldsymbol{\kappa}}}^{\mathbf{T}} \cdot \, {}_{i}\boldsymbol{\kappa} d\boldsymbol{\Omega}
\end{aligned} \tag{87}$$

5.2 Numerical flowchart

Fig. 4 exhibits the flowchart of the proposed method. This figure consists of "global" and "local" iteration procedures. The global solution is used to trace the equilibrium path of a system, whereas the local solution is used to calculate the stresses and consistent material tangent matrices at each Gauss point. For the former, a hybrid solution strategy (e.g., Gutiérrez 2004, Verhoosel *et al*. 2009) is used, initially with force control and then with energy dissipation-based arc length control; for the latter,

Table 1 Flowchart of the stress update

At time step $t^n \xrightarrow{+\Delta t} t^{n+1}$, if the displacement and nonlocal internal variables of control points after i times of iteration are ${}_i\mathbf{u}_N$ and ${}_i\overline{\boldsymbol{\kappa}}_N$, respectively, then the stress update algorithm at Gaussian point *kgasp* must be conducted as follows:

1) Calculate $d\mathbf{u}_N$ and $d\overline{\boldsymbol{\kappa}}_N$ in accordance with Eq.(86);

2) Update ${}_{i+1}\mathbf{u}_N$ and ${}_{i+1}\overline{\boldsymbol{\kappa}}_N$ in accordance with Eq.(79) and Eq.(80), correspondingly;

3) Calculate ${}_{i+1}\overline{\boldsymbol{\kappa}}$ in accordance with Eq.(74);

4) Calculate ${}_{i+1}\bar{d} = d\left({}_{i+1}\overline{\boldsymbol{\kappa}}\right)$ and $\frac{\mathrm{d}\bar{d}}{\mathrm{d}\overline{\boldsymbol{\kappa}}}$;

5) Calculate $d\boldsymbol{\varepsilon}$ in accordance with Eq.(75);

6) Read ${}_i\boldsymbol{\kappa}$ from the last iteration step;

7) Elastic predictor:

Calculate trial effective stress ${}_{i+1}\overline{\boldsymbol{\sigma}}^{\text{trial}} = {}_i\overline{\boldsymbol{\sigma}} + \mathbf{D}^{\text{e}} d\boldsymbol{\varepsilon}$

Calculate the value of yield function $F\left({}_{i+1}\overline{\boldsymbol{\sigma}}^{\text{trial}}, {}_i\boldsymbol{\kappa}\right)$

If $F < 0$, then update ${}_{i+1}\overline{\boldsymbol{\sigma}} = {}_i\overline{\boldsymbol{\sigma}}$, ${}_{i+1}\boldsymbol{\kappa} = {}_i\boldsymbol{\kappa}$, $\mathbf{D}_{\overline{\sigma}}^{\text{ep}} = \mathbf{D}^{\text{e}}$, $\mathbf{D}_{\kappa}^{\text{ep}} = 0$; afterward, proceed to Step 8;

If $F > 0$, then proceed to Step 8;

8) Plastic corrector:

Use the return mapping algorithm and sub-stepping strategy to update ${}_{i+1}\overline{\boldsymbol{\sigma}}$, ${}_{i+1}\boldsymbol{\kappa}$, $\mathbf{D}_{\overline{\sigma}}^{\text{ep}}$, and $\mathbf{D}_{\kappa}^{\text{ep}}$;

9) Damage corrector:

Update nominal stress ${}_{i+1}\boldsymbol{\sigma} = \left(1 - {}_{i+1}\bar{d}\right) \cdot {}_{i+1}\overline{\boldsymbol{\sigma}}$;

10) Calculate ${}_{i+2}\mathbf{K}_{uu}$, ${}_{i+2}\mathbf{K}_{u\overline{\kappa}}$, ${}_{i+2}\mathbf{K}_{\overline{\kappa}u}$, ${}_{i+2}\mathbf{K}_{\overline{\kappa}\overline{\kappa}}$, and ${}_{i+2}\mathbf{f}_u^{\text{ext}}$, ${}_{i+2}\mathbf{f}_u^{\text{int}}$, ${}_{i+2}\mathbf{f}_{\overline{\kappa}}^{\text{ext}}$, and ${}_{i+2}\mathbf{f}_{\overline{\kappa}}^{\text{int}}$ in accordance with Eq.(87);

11) Check errors in accordance with Eq.(88). If the equation is satisfied, then proceed to Step 12. Otherwise, perform $i = i + 1$ and then return to Step 1;

12) Update the converged displacement and nonlocal internal variables as follows:

${}^{n+1}\mathbf{u}_N = {}_{i+1}\mathbf{u}_N$ and ${}^{n+1}\overline{\boldsymbol{\kappa}}_N = {}_{i+1}\overline{\boldsymbol{\kappa}}_N$

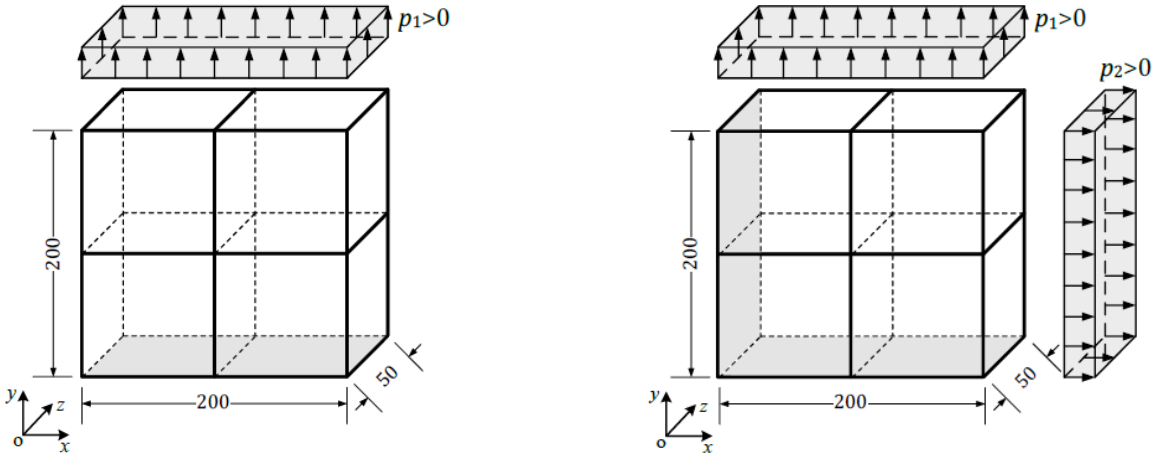

(a) Under uniaxial stress (b) Under biaxial stress

Fig. 5 Isogeometric models of the concrete specimen (unit: mm)

also known as stress updating (Table 1), the solution process is decoupled by splitting operator (e.g., Simo and Ju 1987a, b, Ju 1989) into the following sub-steps: elastic predictor → plastic corrector → damage corrector. The convergence of the plastic corrector is achieved through return mapping algorithm and adaptive sub-stepping strategy; however, other procedures can be exploited, thus avoiding a return mapping and allowing for large load increments (e.g., Areias *et al*. 2013a, Areias *et al*. 2013b, Areias *et al*. 2014, Areias *et al*. 2015, Areias *et al*. 2016a, Areias *et al*. 2016b).

The Newton iteration at the "global" level can be stopped once the following stopping criteria are fulfilled.

$$\begin{aligned} \boldsymbol{R}(\mathbf{f}_u) &= \left\| {}_i\mathbf{f}_u^{\text{ext}} - {}_i\mathbf{f}_u^{\text{int}} \right\| / \left\| {}_i\mathbf{f}_u^{\text{ext}} \right\| \le \mathbf{Tol}_{\mathbf{f}_u} \\ \boldsymbol{R}(\mathbf{u}_N) &= \left\| {}_i\mathbf{u}_N - {}_{i-1}\mathbf{u}_N \right\| / \left\| {}_i\mathbf{u}_N \right\| \le \mathbf{Tol}_{\mathbf{u}_N} \\ \boldsymbol{R}(\overline{\boldsymbol{\kappa}}_N) &= \left\| {}_i\overline{\boldsymbol{\kappa}}_N - {}_{i-1}\overline{\boldsymbol{\kappa}}_N \right\| / \left\| {}_i\overline{\boldsymbol{\kappa}}_N \right\| \le \mathbf{Tol}_{\overline{\boldsymbol{\kappa}}_N} \end{aligned} \tag{88}$$

where the error tolerances are chosen as 0.001.

6. Numerical results

The validations on material level of the proposed damage-plasticity model of concrete are the simulations of uniaxial tension tests of Gopalaratnam and Shah (1985), uniaxial compression tests of Karsan and Jirsa (1969), and biaxial monotonic tension and compression tests of Kupfer *et al*. (1969). The validations on the component level are the

Table 2 Material and solution parameters for the uniaxial tension simulation

E_{0t}(GPa)	ν	ε_{0t}	ε_{ft}	f_{ft}(MPa)	d_{0t}	A_{2t}	B_{3t}	$\Delta\lambda_F$	p_1(MPa)	n_d	$\Delta\tau_{min}(N\cdot m)$	$\Delta\tau_{max}(N\cdot m)$
31	0.18	0.000105	0.00012	3.48	0	$0.7f_{ft}^2$	1.5	1.0	0.1	5	0.0001	1.0

Table 3 Material and solution parameters for the uniaxial compression simulation

E_{0c}(GPa)	ν	ε_{0c}	ε_{fc}	f_{fc}(MPa)	d_{0c}	A_{2c}	B_{3c}	$\Delta\lambda_F$	p_1(MPa)	n_d	$\Delta\tau_{min}(N\cdot m)$	$\Delta\tau_{max}(N\cdot m)$
31	0.18	0.00067	0.002	-27.6	0	0.75	2.0	1.0	-1.0	5	0.0001	5.0

Table 4 Material and solution parameters for the biaxial tension simulation

E_{0t}(GPa)	ν	ε_{0t}	ε_{ft}	f_{ft}(MPa)	d_{0t}	A_{2t}	B_{3t}	$\Delta\lambda_F$	p_1(MPa)	n_d	$\Delta\tau_{min}(N\cdot m)$	$\Delta\tau_{max}(N\cdot m)$
31	0.18	0.000105	0.00012	3.48	0	$0.7f_{ft}^2$	1.5	1.0	0.1	5	0.0001	1.0

Table 5 Material and solution parameters for the biaxial compression simulation

E_{0c}(GPa)	ν	ε_{0c}	ε_{fc}	f_{fc} (MPa)	d_{0c}	A_{2c}	B_{3c}	$\Delta\lambda_F$	p_1(MPa)	n_d	$\Delta\tau_{min}(N\cdot m)$	$\Delta\tau_{max}(N\cdot m)$
31	0.18	0.00067	0.002	-32.8	0	0.75	2.0	1.0	-1.0	5	0.0001	5.0

simulations of the tests of three-point bending single-notched plain concrete beams, four-point bending single-notched plain concrete beams and four-point bending double-notched plain concrete beams.

For all the tested cases, the external load is applied in accordance with the following hybrid scheme. Force control method with load increment factor $\Delta\lambda_F = 1.0$ is used at the beginning stage. Once the number of global iterations exceeds a threshold value of n_d, and no convergent solution is obtained, the dissipation-based arc-length method is activated to trace the subsequent equilibrium path.

6.1 Uniaxial tension and compression simulations

As shown in Fig. 5, the concrete specimen are all 200×200×250 mm, and four first-order linear NURBS solid elements are discretized in space for uniaxial and biaxial simulations respectively.

When simulating uniaxial tension and compression tests of concrete, the boundary conditions of the specimen are treated as follows: (1) all vertical displacements of the control points at $y = 0$ are constrained; (2) uniform load p_1 is applied to the control points at $y = 200$ as an equivalent force. The material and solution parameters used in uniaxial tension simulation are listed in Table 2. Those used in uniaxial compression simulation are listed in Table 3. The parameters are consistent with those adopted in the experiments for comparative analysis.

The stress-strain curves under uniaxial tension and compression obtained from the numerical models are compared with the experimental data presented in Fig. 6. The numerical results agree well with the experimental data of the plastic-hardening and strain-softening characteristics of concrete.

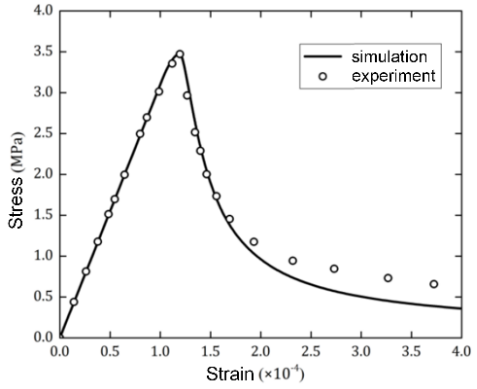

(a) Under uniaxial tension

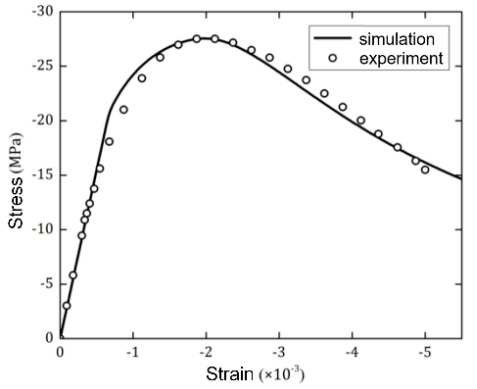

(b) Under uniaxial compression

Fig. 6 Comparison between the stress-strain curves obtained from the numerical models and the experimental data under uniaxial load

6.2 Biaxial tension and compression simulations

When simulating biaxial tension and compression tests of concrete, the boundary conditions of the specimen are treated as follows: (1) the displacements in x-direction and y-direction of the control points at $y = 0$ and $x = 0$ are constrained; (2) uniform load p_1 and p_2 are applied to the control points at $y = 200$ and $x = 200$ as equivalent forces. The material and solution parameters used in biaxial tension simulation and biaxial compression simulation are listed in Table 4 and Table 5, respectively. The parameters are also consistent with those adopted in the experiments for comparative analysis. In order to facilitate the result processing, the normalized parameter $\beta_p = f_{fc}$ is

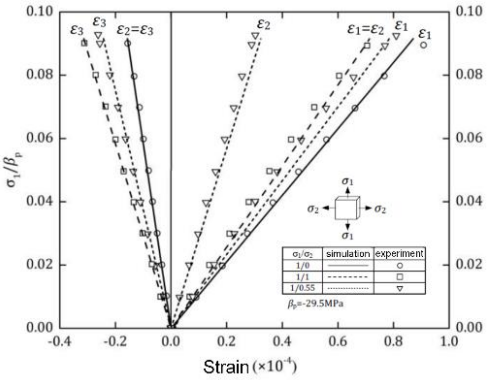

(a) Under biaxial tension

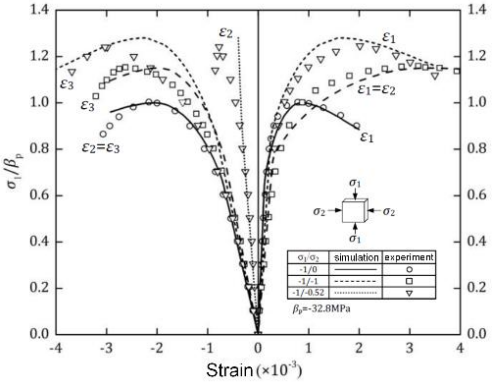

(b) Under biaxial compression

Fig. 7 Comparison between the stress-strain curves obtained from the numerical models and the experimental data under biaxial load

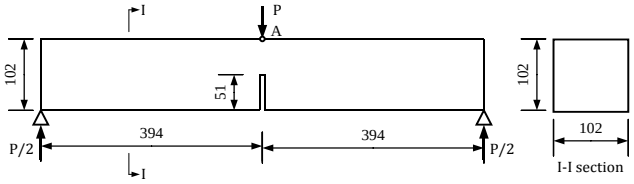

Fig. 8 The geometry of the three-point bending single-notched beam (unit: mm)

introduced.

For biaxial tension, three stress ratios are simulated by reference tests: $\sigma_1/\sigma_2 = 1/0$, $\sigma_1/\sigma_2 = 1/0.55$ and $\sigma_1/\sigma_2 = 1/1$.

For biaxial compression, three stress states are also simulated by reference tests: $\sigma_1/\sigma_2 = -1/0$, $\sigma_1/\sigma_2 = -1/-0.52$ and $\sigma_1/\sigma_2 = -1/-1$.

The stress-strain curves under biaxial tension and compression obtained from the numerical models are compared with the experimental data presented in Fig. 7. The numerical results agree well with the experimental data. And according to the results of ε_2 and ε_3, the model can also simulate the non-linear lateral expansion of concrete caused by Poisson's ratio.

6.3 Three-point bending single-notched beam

A single-notched plain concrete beam under a three-point loading, which has been experimentally tested by Malvar and Warren (1988), must be considered. The predominant failure behavior of the beam is Mode I cracking. Fig. 8 displays the geometrical data and boundary conditions of the beam. Four meshes (denoted by I, II, III, and IV) are generated (Fig. 9). For each mesh, linear and quadratic basis functions are considered, thus indicating that eight numerical models (I-1, II-1, III-1, IV-1 and I-2, II-2, III-2, IV-2) are studied.

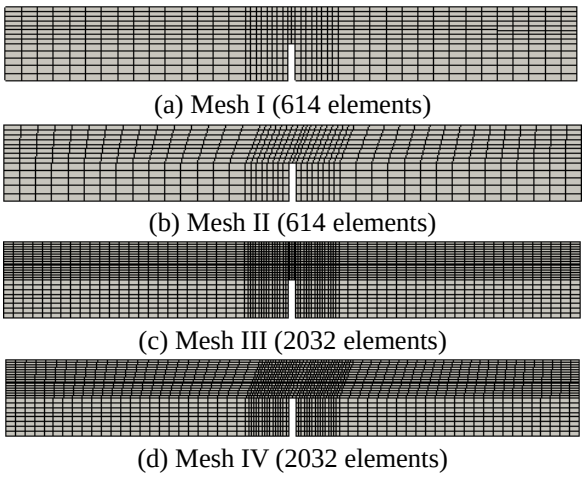

(a) Mesh I (614 elements)

(b) Mesh II (614 elements)

(c) Mesh III (2032 elements)

(d) Mesh IV (2032 elements)

Fig. 9 Isogeometric discretization of the three-point bending single-notched beam

Table 6 and Table 7 lists the material and solution parameters used in the simulation, respectively. All parameters are selected according to the parameters adopted in the experiments. The loading scheme is realized by force control to arc length control: in the initial stage of loading, the vertical downward concentrated force is applied at the mid-span Point A with an increment of 50 KN per step. If the number of iterations of the global solution is more than 5 and the convergence solution is still not obtained, the arc length method based on energy dissipation rate is used to control the load of each step. The characteristic length is regarded as $l_{ch} = 7.5$ mm to obtain a relatively close agreement with the experimental data.

The load-displacement curves of Point A obtained from the eight numerical models are compared with the experimental data presented in Fig. 10. The numerical results agree well with the experimental data in the ascending and descending branches. The load-displacement curves are fairly meshing independent, thereby indicating that the gradient-enhanced formulation used in the present study can eliminate the mesh sensitivity of the traditional damage-plasticity model. Moreover, a quadratic NURBS simulation produces soft results, and the "scatter" is less than that in the case of linear complete basis functions.

It can be found that neither $\bar{\kappa}_c$ nor $\bar{d}_c$ have evolutions, thereby indicating that the failure of the beam is caused by the damage of concrete in tension. Fig. 11 and Fig. 12 illustrate the evolution patterns of $\bar{\kappa}_t$ and $\bar{d}_t$ in Model IV-1, respectively. With continuous loading, $\bar{\kappa}_t$ and $\bar{d}_t$ initiate around the notch tip and then gradually evolve toward the top surface at mid-span. This behavior agrees with the experimental observations. Refined and inclined

Table 6 Material parameters for the three-point bending single-notched beam

E_0(GPa)	v	ε_{0t}	ε_{ft}	f_{ft}(MPa)	ε_{0c}	ε_{fc}	f_{fc}(MPa)	d_0	A_{2t}	B_{3t}	A_{2c}	B_{3c}
21.7	0.2	0.000105	0.00012	2.4	0.00085	0.002	-29	0	$0.1f_{ft}^2$	2.1	0.75	2.0

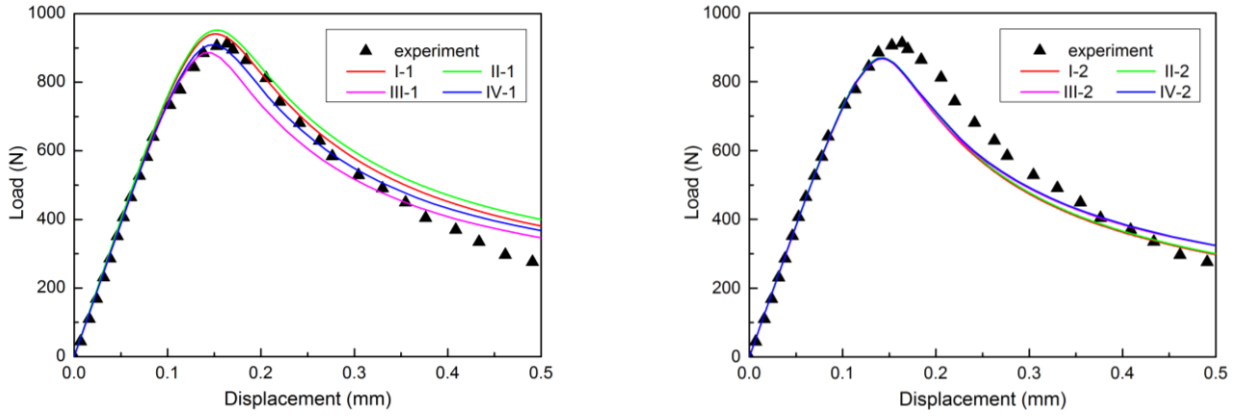

(a) Linear NURBS basis functions (b) Quadratic NURBS basis functions

Fig. 10 Load-vertical displacement curves of Point A obtained from different meshes of the three-point bending single-notched beam

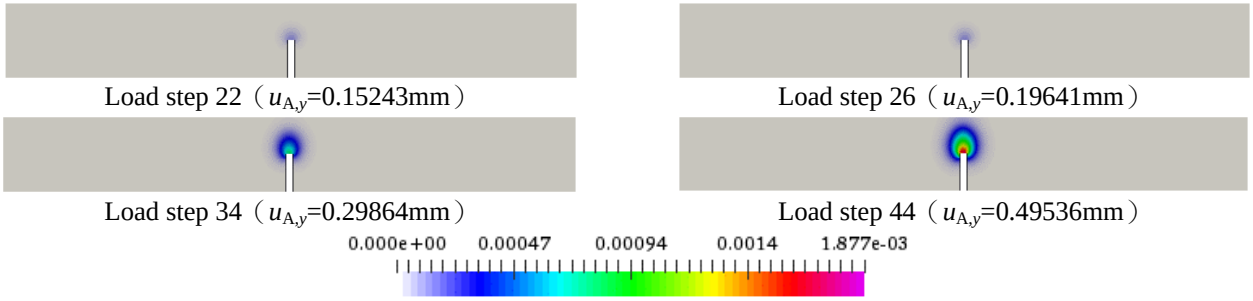

Fig. 11 Evolution pattern of the nonlocal tensile internal variable for the three-point bending single-notched beam

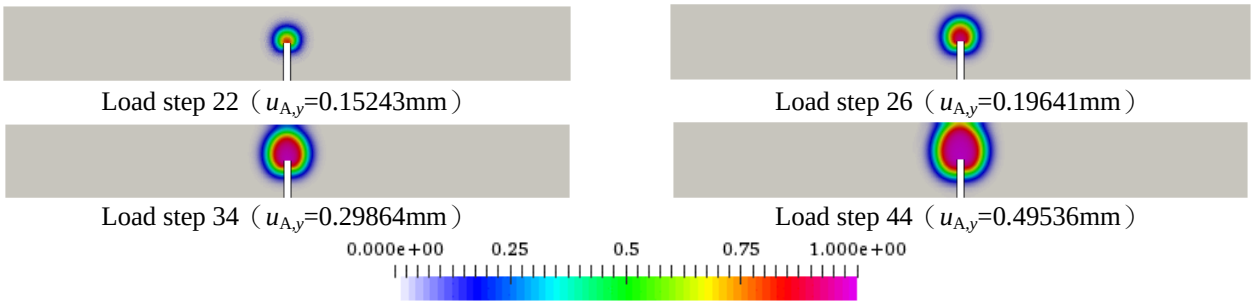

Fig. 12 Evolution pattern of nonlocal tensile damage for the three-point bending single-notched beam

Table 7 Solution parameters for the three-point bending single-notched beam

$\Delta\lambda_F$	n_d	$\Delta\tau_{min}(N\cdot m)$	$\Delta\tau_{max}(N\cdot m)$
1.0	5	0.001	0.009

meshes have no influence on the distribution contour of nonlocal parameters, thus indicating the mesh objectivity of the gradient formulation. Fig. 13 depicts the influence of characteristic length on the load-displacement curves. The results seem slightly independent of the order (linear or quadratic), and the peak load increases with the characteristic length.

6.4 Four-point bending single-notched beam

The second example is a single-notched concrete beam that is subjected to four-point bending that causes mixed-mode cracking (Modes I and II cracking). The experimental results were reported by Arrea and Ingraffea (1982), and numerous computational studies have been conducted with alternative methods (e.g., Rabczuk and Belytschko 2004, Al-Rub and Voyiadjis 2009). Fig. 14 demonstrates the geometrical data and boundary conditions of the beam. The four meshes (I, II, III, and IV) are generated (Fig. 15). For each mesh, linear and quadratic basis functions are considered, thus leading to eight numerical models (I-1, II-1, III-1, IV-1 and I-2, II-2, III-2, IV-2).

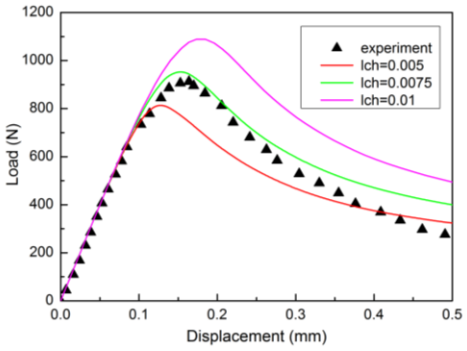

(a) model II-1

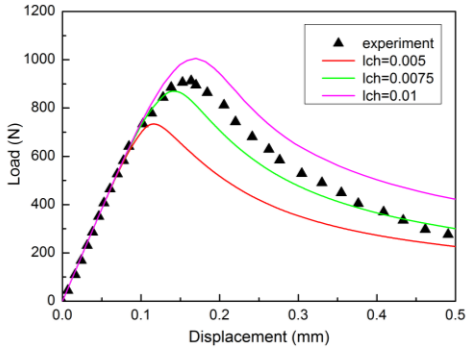

(b) model II-2

Fig. 13 Influence of the characteristic length on the load-displacement curves of Point A for the three-point bending single-notched beam

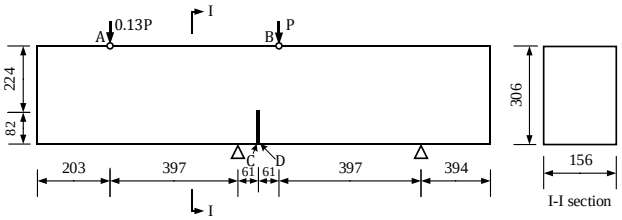

Fig. 14 Geometry of the four-point bending single-notched beam (unit: mm)

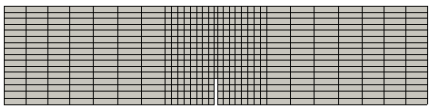

(a) Mesh I (614 elements)

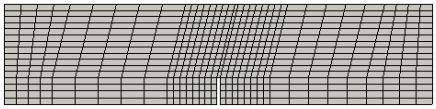

(b) Mesh II (614 elements)

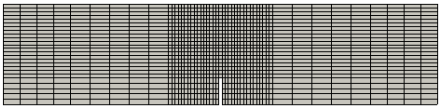

(c) Mesh III (2032 elements)

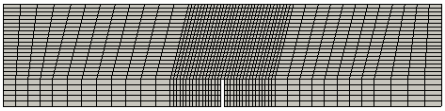

(d) Mesh IV (2032 elements)

Fig. 15 Isogeometric discretization of the four-point bending single-notched beam

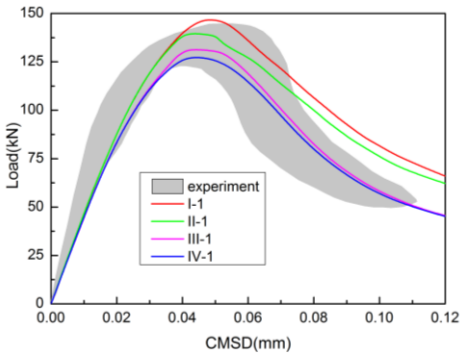

(a) Linear NURBS basis functions

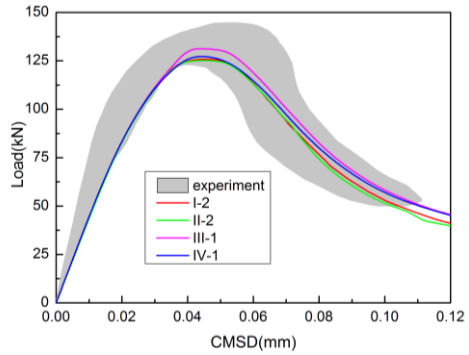

(b) Quadratic NURBS basis

Fig. 16 Load-crack mouth sliding displacement (CMSD) curves of the four-point bending single-notched beam

The material parameters used in the simulation lists in Table 8, the solution parameters are the same as those of three-point bending single-notched beam, and the characteristic length $l_{ch} = 8\,\text{mm}$, which are also consistent with the experimental data. In the initial stage of loading, the vertical downward concentrated forces are applied at Points A and B with the increment of $0.13P$ and P (P=10 kN) per step, respectively. If the number of iterations of the global solution is more than 5 and the convergence solution is still not obtained, the arc length method based on energy dissipation rate is used to control the load of each step.

Fig. 16 exhibits the comparison between the calculated load-CMSD curves and the experimental data. CMSD is defined as the relative vertical displacement between Points C and D, which are located at the two sides of the notch mouth. Figs. 17 and Fig. 18 display the evolution patterns of the nonlocal tensile internal variable $\bar{\kappa}_t$ and nonlocal tensile damage variable $\bar{d}_t$, correspondingly. With continuous loading, $\bar{\kappa}_t$ and $\bar{d}_t$ induce a crack propagation path, which tends to curve away from the original notch tip and move toward the direction of Point B, thereby indicating a typical behavior for a crack subjected to a mixed-mode loading. The distribution contours of $\bar{\kappa}_t$ and $\bar{d}_t$ are not localized into a narrow band when the mesh is refined and are insensitive to mesh alignment, thus showing a mesh objectivity. Considering the previous example, the quadratic NURBS formulation is only slightly sensitive with respect to mesh refinement (Fig. 15). Fig. 19 presents the influence of the characteristic length on the load-CMSD curves. Therefore, the level of peak load increases when the large characteristic length is selected.

Table 8 Material parameters for the four-point bending single-notched beam

E_0(GPa)	v	ε_{0t}	ε_{ft}	f_{ft}(MPa)	ε_{0c}	ε_{fc}	f_{fc}(MPa)	d_0	A_{2t}	B_{3t}	A_{2c}	B_{3c}
24.8	0.18	0.000105	0.00012	2.8	0.00085	0.002	-29	0	$0.05f_{ft}^2$	2.2	0.75	2.0

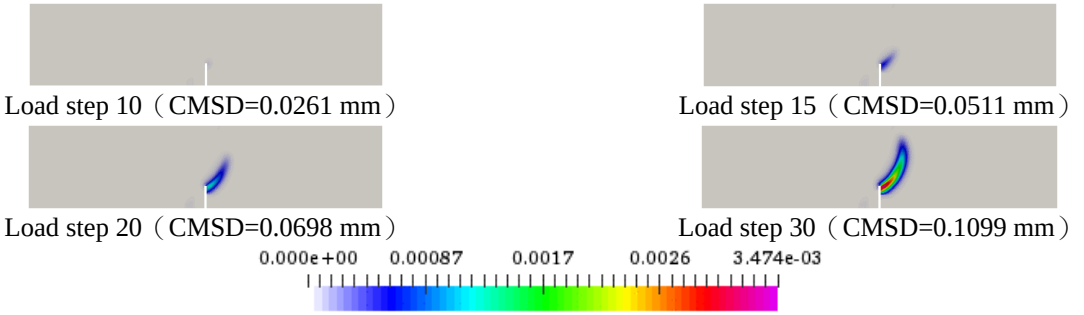

Fig. 17 Evolution pattern of tensile internal variables for the four-point bending single-notched beam

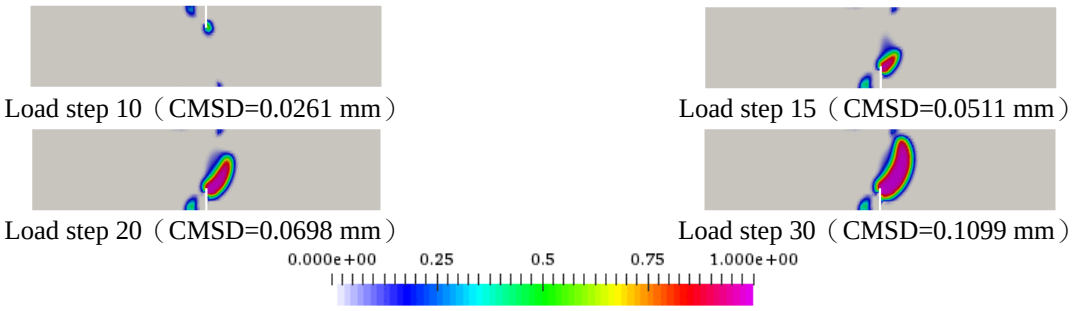

Fig. 18 Evolution pattern of tensile damage for the four-point bending single-notched beam

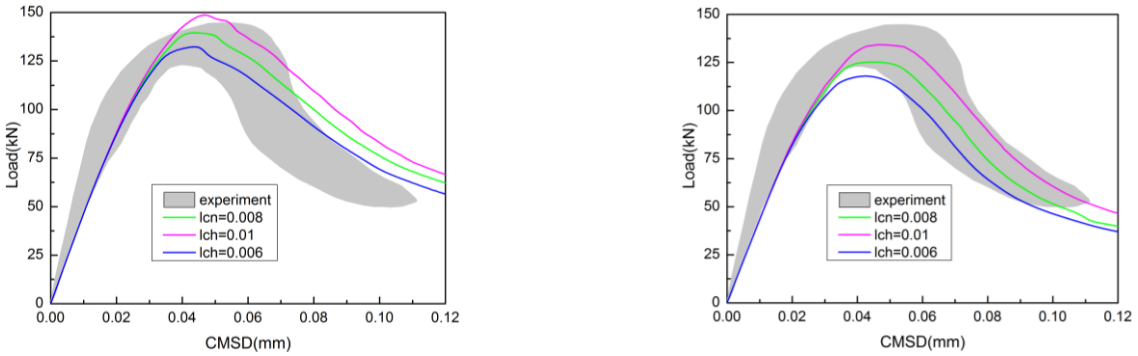

(a) model II-1 (b) model II-2

Fig. 19 Influence of characteristic length on the load-CMSD curves for the four-point bending single-notched beam

Table 9 Material parameters for the four-point bending double-notched beam

E_0(GPa)	v	ε_{0t}	ε_{ft}	f_{ft}(MPa)	ε_{0c}	ε_{fc}	f_{fc}(MPa)	d_0	A_{2t}	B_{3t}	A_{2c}	B_{3c}
27.0	0.18	0.00007	0.00009	2.0	0.00085	0.002	-33.4	0	$0.1f_{ft}^2$	1.9	0.75	2.0

6.5 Four-point bending double-notched beam

The third example investigated here illustrates the use of the proposed approach for analyzing a double-notched concrete beam subjected to four-point bending that causes a mixed-mode cracking (Modes I and II cracking). This problem is more complicated than the second one and has been proposed by Bocca *et al.* (1990). It is also a classical benchmark problem for fracture, which has been studied by several authors (e.g., Rabczuk and Belytschko 2004, Rabczuk and Zi 2007). Fig. 20 depicts the geometrical data and boundary conditions of the beam. Two meshes (I and II) are generated (Fig. 21). For each mesh, linear and quadratic basis functions are considered; thus, four numerical models (I-1, II-1 and I-2, II-2) are studied.

Table 9 and Table 10 lists the material and solution parameters used in the simulation, with the characteristic length $l_{ch} = 3$ mm. In the initial stage of loading, the vertical downward concentrated forces are applied at Points A and B with the increment of 0.2P and P (P=2/1.2 kN) per step, respectively. If the number of iterations of the global solution is more than 5 and the convergence solution is still not obtained,

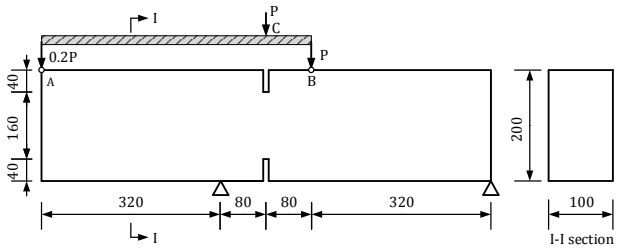

Fig. 20 The geometry of the four-point bending double-notched beam (unit: mm)

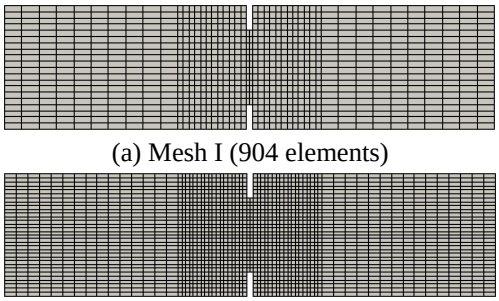

(a) Mesh I (904 elements)

(b) Mesh II (2152 elements)

Fig. 21 Isogeometric discretization of the four-point bending double-notched beam

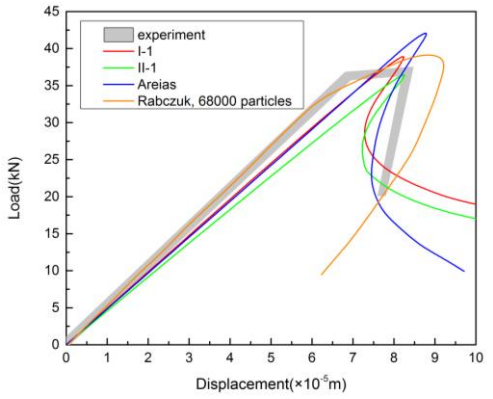

(a) Linear NURBS basis functions

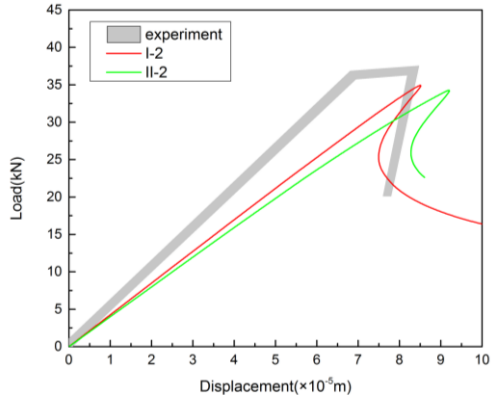

(b) Quadratic NURBS basis functions

Fig. 22 Load-vertical displacement curves of Point C obtained from the different meshes of the four-point bending double-notched beam

the arc length method based on energy dissipation rate is used to control the load of each step.

Table 10 Solution parameters for the four-point bending double-notched beam

$\Delta\lambda_F$	n_d	$\Delta\tau_{min}(N\cdot m)$	$\Delta\tau_{max}(N\cdot m)$
1.0	5	0.001	0.09

Fig. 22 presents the comparison between the calculated load-vertical displacement curves of Point C and the experimental data. Fig. 19(a) demonstrates the results obtained by Areias *et al.* (2015) and Rabczuk and Belytschko (2004) for the purpose of comparison. The rigid loading beam is not simulated in the test; thus, the vertical displacement of Point C can only be estimated by averaging the vertical displacements of Points A and B. Fig. 23 and Fig. 24 exhibits the evolution patterns of nonlocal tensile internal variable $\bar{\kappa}_t$ and nonlocal tensile damage variable $\bar{d}_t$. Internal variables $\bar{\kappa}_t$ and $\bar{d}_t$ induce a crack path, which curves away from the original notch tip that agrees with the experimental observation. Fig. 25 displays the influence of characteristic length on the load-displacement curves. Consistent with the results in previous subsections, the peak load increases with the characteristic length.

7. Conclusions

Isogeometric analysis method can provide the possibility of integrated computer-aided design and computer-aided engineering into a uniform process. But the use of this technology on the advanced analysis of engineering structures is still rare. This study presents a damage-plasticity model for concrete in the context of the IGA. Since the traditional local models usually suffer from ill-posed problems like mesh dependency, an implicit gradient formulation is introduced to the plastic-damage model as the regularization remedy. The proposed method is validated on material level and component level by the plain concrete benchmark problems. The results are presented as follows:

- By comparing the numerical results with the experimental data at the same condition, the feasibility of the proposed model and the mixed-mode fracture of concrete is proofed;
- The global load-displacement (or CMSD) curves and damage evolution patterns exhibit no evident mesh dependence, thereby indicating that the gradient-enhanced formulation can regularize ill-posed problems. Moreover, the "scatter" in the load-deflection curves for coarse meshes is less pronounced in the quadratic IGA formulation than in the linear formulation.
- The level of peak load increases once a large characteristic length is selected.
- The gradient formulation for the internal variables only leads to the nonlocal damage of concrete, and the plasticity part remains local. Therefore, the presented approach may serve only as a partial localization limiter. The ‘‘over-nonlocal" formulation (e.g., Vermeer and Brinkgreve 1994; Grassl and Jirasek 2006b; Poh and Swaddiwudhipong 2009) can be used to remedy this situation.

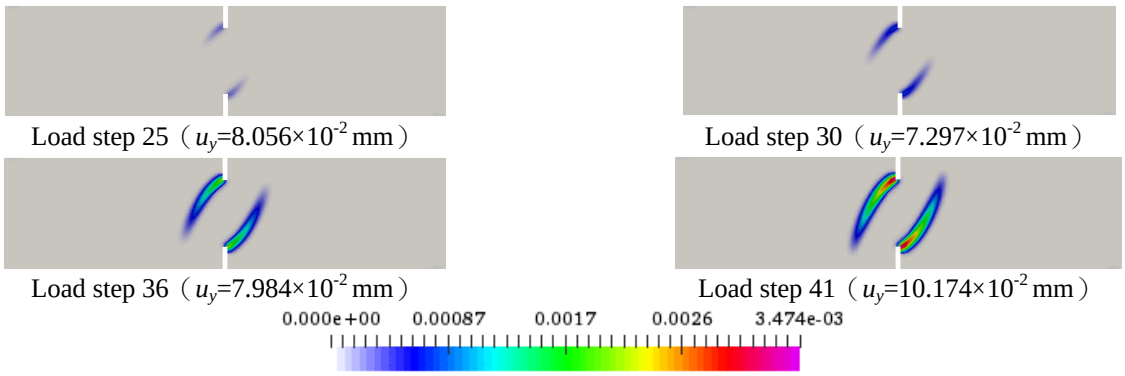

Fig. 23 Evolution pattern of tensile internal variables for the four-point bending double-notched beam

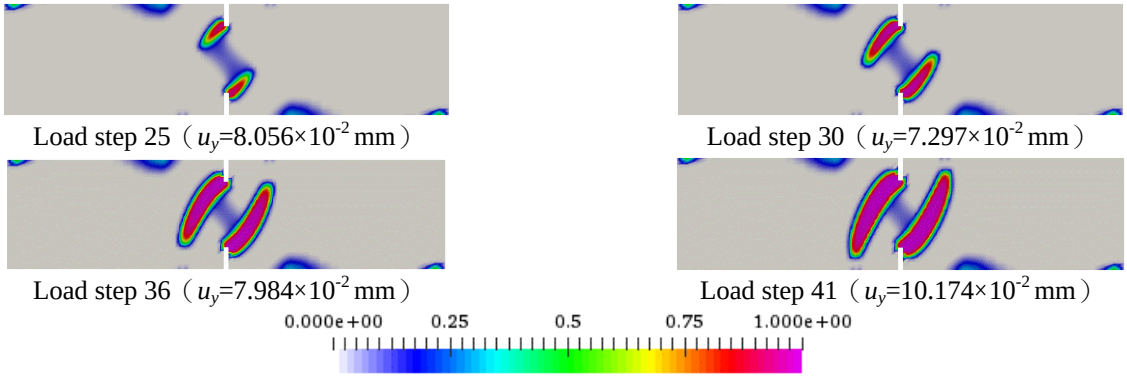

Fig. 24 Evolution pattern of tensile damage for the four-point bending double-notched beam

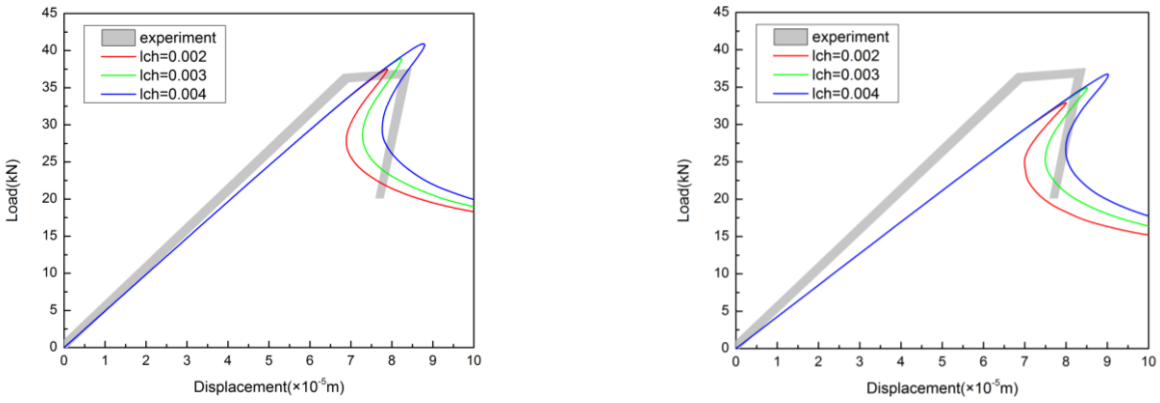

(a) model II-1 (b) model II-2

Fig. 25 Influence of characteristic length on the load-vertical displacement curves of Point C for the four-point bending double-notched beam

Considering the advantages of IGA in modeling geometries accurately, this approach can be extended to the reinforced concrete with complex curved shapes of the reinforcement. This aspect can be investigated in future research.

Acknowledgments

The research described in this paper was financially supported by the National Natural Science Foundation of China and the Chinese Scholarship Council, whose precious help is gratefully acknowledged.

References

Aifantis, E.C. (1984), "On the microstructural origin of certain inelastic models", *J. Eng. Mater. Technol.*, **106**(4), 326-330.

Al-Rub, R.K.A. and Voyiadjis, G.Z. (2009), "Gradient-enhanced coupled plasticity-anisotropic damage model for concrete fracture: computational aspects and applications", *Int. J. Damage Mech.*, **18**(2), 115-154.

Anitescu, C., Jia, Y., Zhang, Y.J. and Rabczuk, T. (2015), "An isogeometric collocation method using superconvergent points", *Comput. Meth. Appl. Mech. Eng.*, **284**, 1073-1097.

Areias, P., Msekh, M.A. and Rabczuk, T. (2016a), "Damage and fracture algorithm using the screened Poisson equation and local remeshing", *Eng. Fract. Mech.*, **158**, 116-143.

Areias, P., Rabczuk, T. and Camanho, P.P. (2013a), "Initially rigid

cohesive laws and fracture based on edge rotations", *Comput. Mech.*, **52**(4), 931-947.
Areias, P., Rabczuk, T. and Camanho, P.P. (2014), "Finite strain fracture of 2D problems with injected anisotropic softening elements", *Theor. Appl. Fract. Mech.*, **72**, 50-63.
Areias, P., Rabczuk, T. and Dias-Da-Costa, D. (2013b), "Element-wise fracture algorithm based on rotation of edges", *Eng. Fract. Mech.*, **110**(3), 113-137.
Areias, P., Rabczuk, T. and Sá, J.C.D. (2016b), "A novel two-stage discrete crack method based on the screened Poisson equation and local mesh refinement", *Comput. Mech.*, 1-16.
Areias, P., Reinoso, J., Camanho, P. and Rabczuk, T. (2015), "A constitutive-based element-by-element crack propagation algorithm with local mesh refinement", *Comput. Mech.*, **56**(2), 1-25.
Arrea, M. and Ingraffea, A.R. (1982), "Mixed-mode crack propagation in mortar and concrete", Department of Structural Engineering, Cornell University, Ithaca, NY.
Bazant, Z.P. (1991), "Why continuum damage is nonlocal: micromechanics arguments", *J. Eng. Mech.*, **117**(5), 1070-1087.
Bazant, Z.P. and Jirasek, M. (2002), "Nonlocal integral formulations of plasticity and damage: survey of progress", *J. Eng. Mech.*, **128**(11), 1119-1149.
Bazant, Z.P. and Pijaudier-Cabot, G. (1988), "Nonlocal continuum damage, localization instability and convergence", *J. Appl. Mech.*, **55**(2), 287-293.
Bazant, Z.P. and Pijaudier-Cabot, G. (1989), "Measurement of characteristic length of nonlocal continuum", *J. Eng. Mech.*, **115**(4), 755-767.
Bazant, Z.P., Belytschko, T.B. and Chang, T.P. (1984), "Continuum theory for strain-softening", *J. Eng. Mech.*, **110**(12), 1666-1692.
Bazilevs, Y., Calo, V.M., Hughes, T.J.R. and Zhang, Y. (2008), "Isogeometric fluid-structure interaction: theory, algorithms, and computations", *Comput. Mech.*, **43**(1), 3-37.
Bocca, P., Carpinteri, A. and Valente, S. (1990), "Size effects in the mixed mode crack propagation: softening and snap-back analysis", *Eng. Fract. Mech.*, **35**(1-3), 159-170.
Borden, M.J., Hughes, T.J.R., Landis, C.M. and Verhoosel, C.V. (2014), "A higher-order phase-field model for brittle fracture: Formulation and analysis within the isogeometric analysis framework", *Comput. Meth. Appl. Mech. Eng.*, **273**(5), 100-118.
Bui, T.Q., Hirose, S., Zhang, C., Rabczuk, T., Wu, C.T., Saitoh, T. and Lei, J. (2016), "Extended isogeometric analysis for dynamic fracture in multiphase piezoelectric/piezomagnetic composites", *Mech. Mater.*, **97**, 135-163.
Chen, A.C.T. and Chen, W.F. (1975), "Constitutive relations for concrete", *J. Eng. Mech.*, **101**, Proc. Paper 11529.
Cottrell, J.A., Reali, A., Bazilevs, Y. and Hughes, T.J.R. (2006), "Isogeometric analysis of structural vibrations", *Comput. Meth. Appl. Mech. Eng.*, **195**(41-43), 5257-5296.
Darwin, D. and Pecknold, D.A. (1977), "Nonlinear biaxial stress-strain law for concrete", *J. Eng. Mech.*, **103**(EM2), 12839.
de Borst, R. and Pamin, J. (1996), "Some novel developments in finite element procedures for gradient-dependent plasticity", *Int. J. Numer. Meth. Eng.*, **39**(14), 2477-2505.
de Borst, R., Benallal, A. and Heeres, O.M. (1996), "A gradient-enhanced damage approach to fracture", *Le Journal de Physique IV*, **06**(C6), 491-502.
de Borst, R., Hughes, T.J.R., Scott, M.A. and Verhoosel, C.V. (2011), "Isogeometric failure analysis", *Multiscale and Multiphysics Processes in Geomechanics*, Springer, 113-116.
Dorgan, R.J. and Voyiadjis, G.Z. (2006), "A mixed finite element implementation of a gradient-enhanced coupled damage-plasticity model", *Int. J. Damage Mech.*, **15**(3), 201-235.
Elwi, A.A. and Murray, D.W. (1979), "A 3D hypoelastic concrete constitutive relationship", *J. Eng. Mech. Div.*, **105**(4), 623-641.
Engelen, R.A.B., Geers, M.G.D. and Baaijens, F.P.T. (2003), "Nonlocal implicit gradient-enhanced elasto-plasticity for the modelling of softening behaviour", *Int. J. Plast.*, **19**(4), 403-433.
Eringen, A.C. and Edelen, D.G.B. (1972), "On nonlocal elasticity", *Int. J. Eng. Sci.*, **10**(3), 233-248.
Feist., C. and Hofstetter, G. (2007), "Validation of 3d crack propagation in plain concrete. Part I: Experimental investigation - the pct3d test", *Comput. Concrete*, **4**(1), 49-66.
Gopalaratnam, V.S. and Shah, S.P. (1985), "Softening response of plain concrete in direct tension", *ACI J. Proc.*, **82**(3), 310-323.
Grassl, P. and Jirasek, M. (2006a), "Damage-plastic model for concrete failure", *Int. J. Solid. Struct.*, **43**(22), 7166-7196.
Grassl, P. and Jirasek, M. (2006b), "Plastic model with non-local damage applied to concrete", *Int. J. Numer. Anal. Meth. Geomech.*, **30**(1), 71-90.
Gutiérrez, M.A. (2004), "Energy release control for numerical simulations of failure in quasi-brittle solids", *Commun. Numer. Meth. Eng.*, **20**(1), 19-29.
Han, D.J. and Chen, W.F. (1985), "A nonuniform hardening plasticity model for concrete materials", *Mech. Mater.*, **4**(3), 283-302.
Hossain, K.M.A. and Olufemi, O.O. (2004), "Computational optimization of a concrete model to simulate membrane action in RC slabs", *Comput. Concrete*, **1**(3), 325-354.
Hughes, T.J.R., Cottrell, J.A. and Bazilevs, Y. (2005), "Isogeometric analysis: CAD, finite elements, NURBS, exact geometry and mesh refinement", *Comput. Meth. Appl. Mech. Eng.*, **194**(39-41), 4135-4195.
Jelic., I., Pavlovic, M.N. and Kotsovos, M.D. (2004). "Performance of structural-concrete members under sequential loading and exhibiting points of inflection", *Comput. Concrete*, **1**(1), 99-113.
Jia, Y., Anitescu, C., Ghorashi, S.S. and Rabczuk, T. (2015), "Extended isogeometric analysis for material interface problems", *IMA J. Appl. Math.*, **80**(3), 608-633..
Jirasek, M. (1998), "Nonlocal models for damage and fracture: comparison of approaches", *Int. J. Solid. Struct.*, **35**(31), 4133-4145.
Ju, J.W. (1989), "On energy-based coupled elastoplastic damage theories: Constitutive modeling and computational aspects", *Int. J. Solid. Struct.*, **25**(7), 803-833.
Karsan, I.D. and Jirsa, J.O. (1969), "Behavior of concrete under compressive loadings", *J. Struct. Div.*, **95**(12), 2543-2563
Kröner, E. (1967), "Elasticity theory of materials with long range cohesive forces", *Int. J. Solid. Struct.*, **3(**5), 731-742.
Kupfer, H., Hilsdorf, H.K. and Rusch, H. (1969), "Behavior of concrete under biaxial stresses", *ACI J. Proc.*, **66**(8), 656-666.
Lee, J. and Fenves, G. (1998), "Plastic-damage model for cyclic loading of concrete structures", *J. Eng. Mech.*, **124**(8), 892-900.
Loland, K.E. (1980), "Continuous damage model for load-response estimation of concrete", *Cement Concrete Res.*, **10**(3), 395-402.
Lubliner, J., Oliver, J., Oller, S. and Onate, E. (1989), "A plastic-damage model for concrete", *Int. J. Solid. Struct.*, **25**(3), 299-326.
Malvar, L.J. and Warren, G.E. (1988), "Fracture energy for three-point-bend tests on single-edge-notched beams", *Exp. Mech.*, **28**(3), 266-272.
Mazars, J. and Pijaudier-Cabot, G. (1989), "Continuum damage theory-application to concrete", *J. Eng. Mech.*, **115**(2), 345-365.
Miehe, C., Welschinger, F. and Hofacker, M. (2010), "Thermodynamically consistent phase-field models of fracture: Variational principles and multi-field FE implementations", *Int. J. Numer. Meth. Eng.*, **83**(10), 1273-1311.
Nguyen, V.P., Anitescu, C., Bordas, S.P.A. and Rabczuk, T. (2015), "Isogeometric analysis: An overview and computer

implementation aspects", *Math. Comput. Simul.*, **117**, 89-116.
Ozbolt, J., Kozar, I. and Periškić, G. (2007), "Three-dimensional FE analysis of headed stud anchors exposed to fire", *Comput. Concrete*, **2**(4), 249-266.
Pamin, J.K. (1994), "Gradient-dependent plasticity in numerical simulation of localization phenomena", TU Delft, Delft University of Technology.
Papadakis., V.G., Efstathiou., M.P. and Apostolopoulos., C.A. (2007), "I Computer-aided approach of parameters influencing concrete service life and field validation", *Comput. Concrete*, **4**(1), 1-18.
Peerlings, R.H.J., de Borst, R., Brekelmans, W.A.M. and de Vree, J.H.P. (1996a), "Gradient enhanced damage for quasi-brittle materials", *Int. J. Numer. Meth. Eng.*, **39**(19), 3391-3403.
Peerlings, R.H.J., De Borst, R., Brekelmans, W.A.M., De Vree, J.H.P. and Spee, I. (1996b), "Some observations on localisation in non-local and gradient damage models", *Eur. J. Mech. A: Solid.*, **15**(6), 937-953.
Pijaudier-Cabot, G. and Bazant, Z.P. (1987), "Nonlocal damage theory", *J. Eng. Mech.*, **113**(10), 1512-1533.
Poh, L.H. and Swaddiwudhipong, S. (2009), "Over-nonlocal gradient enhanced plastic-damage model for concrete", *Int. J. Solid. Struct.*, **46**(25), 4369-4378.
Rabczuk, T. and Belytschko, T. (2007), "A three-dimensional large deformation meshfree method for arbitrary evolving cracks", *Comput. Meth. Appl. Mech. Eng.*, **196**(29-30), 2777-2799.
Rabczuk, T. and Eibl, J. (2003), "Simulation of high velocity concrete fragmentation using SPH/MLSPH", *Int. J. Numer. Meth. Eng.*, **56**(10), 1421-1444.
Rabczuk, T. and Eibl, J. (2006), "Modelling dynamic failure of concrete with meshfree methods", *Int. J. Impact Eng.*, **32**(11), 1878-1897.
Rabczuk, T., Akkermann, J. and Eibl, J. (2005), "A numerical model for reinforced concrete structures", *Int. J. Solid. Struct.*, **42**(5), 1327-1354.
Rots, J.G., Nauta, P.G., Kuster, G.M.A. and Blaauwendraad, J. (1985), "Smeared crack approach and fracture localization in concrete", *Heron*, **30**(1), 1985.
Saritas, A. and Filippou, F.C. (2009), "Numerical integration of a class of 3d plastic-damage concrete models and condensation of 3d stress-strain relations for use in beam finite elements", *Eng. Struct.*, **31**(10), 2327-2336.
Simo, J.C. and Ju, J.W. (1987a), "Strain- and stress-based continuum damage models - I. Formulation", *Int. J. Solid. Struct.*, **23**(7), 821-840.
Simo, J.C. and Ju, J.W. (1987b), "Strain- and stress-based continuum damage models - II. Computational aspects", *Int. J. Solid. Struct.*, **23**(7), 841-869.
Stroeven., P., Hu., J. and Stroeven, M. (2009), "On the usefulness of discrete element computer modeling of particle packing for material characterization in concrete technology", *Comput. Concrete*, **6**(2), 133-153.
Thai, T.Q., Rabczuk, T., Bazilevs, Y. and Meschke, G. (2016), "A higher-order stress-based gradient-enhanced damage model based on isogeometric analysis", *Comput. Meth. Appl. Mech. Eng.*, **304**, 584-604.
Verhoosel, C.V., Remmers, J.J.C. and Gutiérrez, M.A. (2009), "A dissipation-based arc-length method for robust simulation of brittle and ductile failure", *Int. J. Numer. Meth. Eng.*, **77**(9), 1290-1321.
Verhoosel, C.V., Scott, M.A., Hughes, T.J.R. and De Borst, R. (2011), "An isogeometric analysis approach to gradient damage models", *Int. J. Numer. Meth. Eng.*, **86**(1), 115-134.
Vermeer, P.A. and Brinkgreve, R.B.J. (1994), "A new effective non-local strain measure for softening plasticity", *Localization and Bifurcation Theory for Soils and Rocks*, 89-100.
Voyiadjis, G.Z., Taqieddin, Z.N. and Kattan, P.I. (2008), "Anisotropic damage-plasticity model for concrete", *Int. J. Plast.*, **24**(10), 1946-1965.
Yu, H.X. and Wu, J.H. (2009), "An elastoplastic damage constitutive model for concrete based on undamaged state", *Eng. Mech.*, **26**(10), 79-86. (in Chinese)
Zhu, H., Wang, Q. and Zhuang, X. (2016), "A nonlinear semi-concurrent multiscale method for fractures", *Int. J. Impact Eng.*, **87**, 65-82.
Zhuang, X., Augarde, C.E. and Mathisen, K.M. (2012), "Fracture modeling using meshless methods and level sets in 3D: Framework and modeling", *Int. J. Numer. Meth. Eng.*, **92**(11), 969-998.
Zhuang, X., Cai, Y. and Augarde, C. (2014), "A meshless sub-region radial point interpolation method for accurate calculation of crack tip fields", *Theor. Appl. Fract. Mech.*, **69**(2), 118-125.

CC